Articles in PresS. J Neurophysiol (December 27, 2002). 10.1152/jn.00955.2002

From Subthreshold to Firing-Rate Resonance

Magnus J. E. Richardson[1,2], Nicolas Brunel[3] and Vincent Hakim[1]

[1] Laboratoire de Physique Statistique, Ecole Normale Supérieure,
24 rue Lhomond 75231, Paris Cedex 05, France

[2] Laboratory of Computational Neuroscience
Brain and Mind Institute, EPFL
CH 1015, Lausanne, Switzerland

[3] CNRS, NPSM, Université René Descartes,
45 rue des Saints Pères 75270 Paris Cedex 06, France

Running head: From Subthreshold to Firing-Rate Resonance

Corresponding author: Magnus J. E. Richardson
Address: Laboratory of Computational Neuroscience
Brain and Mind Institute, EPFL
CH 1015, Lausanne, Switzerland
Tel: +41 (0) 1 21 693 5280
Fax: +41 (0) 1 21 693 5263
E-mail: Magnus.Richardson@epfl.ch

Keywords: subthreshold resonance, oscillations, neuronal models, noise.

Abstract:

Many types of neurons exhibit subthreshold resonance. However, little is known about whether this frequency preference influences spike emission. Here, the link between subthreshold resonance and firing rate is examined in the framework of conductance-based models. A classification of the subthreshold properties of a general class of neurons is first provided. In particular, a class of neurons is identified in which the input impedance exhibits a suppression at a non-zero low frequency as well as a peak at higher frequency. The analysis is then extended to the effect of subthreshold resonance on the dynamics of the firing rate. The considered input current comprises a background noise term, mimicking the massive synaptic bombardment *in vivo*. Of interest is the modulatory effect an additional weak oscillating current has on the instantaneous firing rate. When the noise is weak and firing regular, the frequency most preferentially modulated is the firing rate itself. Conversely, when the noise is strong and firing irregular, the modulation is strongest at the subthreshold resonance frequency. These results are demonstrated for two specific conductance-based models and for a generalization of the integrate-and-fire model that captures subthreshold resonance. They suggest that resonant neurons are able to communicate their frequency preference to post-synaptic targets when the level of noise is comparable to that prevailing *in vivo*.

Oscillations have long been observed in neuronal structures (Adrian and Matthews 1934) but their role, mechanisms and interplay with single neuron biophysical characteristics have only recently been submitted to detailed scrutiny. Experiments have tested the response of neurons to oscillating current injection. Subthreshold resonance, in which the response of the induced oscillating voltage peaks at a preferred input frequency, has been found in inferior olive neurons (Llinás and Yarom 1986; Lampl and Yarom 1993; Lampl and Yarom 1997; De Zeeuw et al. 1998), trigeminal root ganglion neurons (Puil et al. 1986), thalamic neurons (Jahnsen and Karnup 1994; Puil et al. 1994; Hutcheon et al. 1994), neocortical neurons (Llinás et al. 1991; Gutfreund et al. 1995; Hutcheon et al. 1996b; Dickson et al. 2000) and in both hippocampal CA1 pyramidal cells (Leung and Yu 1998; Pike et al. 2000) and interneurons (Pike et al. 2000). Many of these structures are known to support oscillations *in vivo*, suggesting an interplay between single-cell frequency preference and oscillations at the network level. Most of the recorded neurons show a single peak at a finite frequency in their voltage response. However, some interneurons of the hippocampus show a more complex response, with a trough at low frequency followed by a peak at higher frequencies (Pike et al. 2000). Though a great deal of effort has been directed at understanding the input properties of resonant neurons, surprisingly little attention has been addressed to the effect of subthreshold resonance on the temporal properties of the firing rate. This is despite the common assumption that the presence of resonant neurons might provide a stabilizing influence on oscillations at the level of the network.

It is known from Hodgkin and Huxley (1952) and many studies since (see e.g. Mauro et al. 1970; Koch 1984; Rinzel and Ermentrout 1989; Hutcheon et al. 1994; Gutfreund et al. 1995; White et al. 1995; Hutcheon et al. 1996a) that the resonance properties of neurons can be related to their ionic channel characteristics through a mathematical linearization of the corresponding conductance-based description. Several scenarios involving voltage-gated ionic currents have been shown to generate resonant behavior (for a review see Hutcheon and Yarom 2000). Reduced two-variable descriptions have proven useful as a mathematical tool to study these and other neuronal properties (Rinzel and Ermentrout 1989; Gutfreund et al. 1995; White et al. 1995; Hutcheon et al. 1996a).

In the first part of this paper, a systematic classification of two-variable models is provided. The analysis highlights the possible types of subthreshold behavior associated with different neuronal characteristics. The results can be summarized in a graphical description. The change of membrane properties as the neuron is depolarized towards threshold is represented by trajectories crossing boundaries separating different types of behavior (e.g. passive from resonant). This description is illustrated with two conductance-based model neurons. More complex types of resonance cannot be described by a two-variable model. For this reason, a three-variable model, which exhibits a richer repertoire of behaviors, is also analyzed. A parameter region is identified with a suppression as well as a resonance in the impedance curve, a feature recently observed experimentally in hippocampal fast-spiking interneurons (Pike et al. 2000).

In the second part of the paper, the circumstances are examined in which a resonant

neuron can communicate its subthreshold frequency preference through the dynamics of its firing rate. This property of resonant neurons manifests itself as a preferential amplification of input signals that are at the resonant frequency, and requires an analysis of how the firing rate is modulated by an oscillatory current. To this end, the two-variable approach is extended to include spike emission, providing a *generalized integrate-and-fire* or *GIF* model. The model captures a wide range of subthreshold dynamics with a simplified firing and reset mechanism. The firing-rate dynamics of this model, as well as two specific conductance-based models which exhibit a subthreshold resonance, are studied in detail. The crucial role that noise plays in shaping the response is highlighted.

MATERIALS AND METHODS

Glossary

v	deviation of the membrane potential from the holding potential (mV).
C or C_M	membrane capacity (nF).
g	effective leak conductance (μS).
w or w_1	auxiliary variable characterizing the membrane dynamics (mV).
τ_1	time scale of the dynamics of the w variable (ms).
g_1	conductance measuring the membrane potential variation resulting from a change of w (μS).
α	dimensionless parameter proportional to leak conductance g.
β	dimensionless parameter proportional to conductance g_1.
w_2	second auxiliary variable (mV).
g_2	analogous to g_1 for the second variable w_2 (μS).
I_{app}	total applied external current (nA).
I_{syn}	synaptic current (nA).
g_{eo} and g_{io}	average excitatory and inhibitory total synaptic conductances (μS).
σ_e and σ_i	magnitude of excitatory and inhibitory synaptic noise (μS).
τ_e and τ_i	correlation timescales of the excitatory and inhibitory synaptic noise (ms).
I_N	magnitude of the fluctuations of synaptic current (nA).
I_0	constant (DC) current (nA).
I_1	magnitude of oscillatory current (nA).
f	frequency of injected current (Hz).
σ_V	strength of the synaptic noise as measured by the resulting amplitude of membrane potential fluctuations (mV).
$Z(f)$	cell impedance for an injected current of frequency f ($M\Omega$).
f_R	resonant frequency corresponding to a maximum of the amplitude of $Z(f)$ (Hz).
f_0	natural frequency of the membrane potential damped oscillations (Hz).
Q	strength of the resonance peak (dimensionless).

r_0	average spike rate (Hz).
$r_1(f)$	magnitude of oscillatory component in spike rate induced by injected oscillatory current (Hz).
$\|A(f)\|$	signal gain (Hz/nA).
$\phi(f)$	phase of oscillatory component in spike rate with respect to oscillatory current (deg).
v_θ	threshold for spike emission for the GIF model (defined in Methods) (mV)
v_r	membrane potential reset after spike emission for the GIF model (defined in Methods) (mV)

Linearization of conductance based models

The starting point for the analysis in this paper is the conductance-based Hodgkin-Huxley formalism. The state of a neuron is described by a potential difference V across a membrane with a capacitance C_M, a set of trans-membrane currents I_{mem} (comprising the leak and various active ionic currents), a synaptic current I_{syn} (to be described below) and an applied current I_{app}

$$C_M \frac{dV}{dt} = -I_{mem} - I_{syn} + I_{app}. \tag{1}$$

The active ionic currents comprise both activation and inactivation variables x_k where $k = 1, \ldots, N$ counts over all the variables that obey equations of the form

$$\tau_k(V)\frac{dx_k}{dt} = x_{k,\infty}(V) - x_k \tag{2}$$

where both the relaxation times $\tau_k(V)$ and the steady-state values $x_{k,\infty}(V)$ are functions of the membrane voltage.

Below threshold for action potential generation, equations (1) and (2) can be linearized around a holding voltage V^* (see e.g. Koch 1999, chapter 10, and refs therein). For the sake of simplicity the notation X^* will be used to denote the quantity X evaluated at $V = V^*$. Linearization of the equation set (1) and (2) allows for a direct categorization of the range of behavior that a neuron exhibits in its response to small input currents, for example the response to an oscillating or square-pulse current considered here. The linearized equations will also provide the basis for a generalization of the integrate-and-fire model, to be described at the end of this section. The linear equations can be written in the following form

$$\begin{aligned} C_M \frac{dv}{dt} &= -g_M v - \sum_{k=1}^{N} g_k w_k - I_{syn} + I_{app} \\ \tau_k \frac{dw_k}{dt} &= v - w_k \quad \text{where } k = 1, \cdots, N \end{aligned} \tag{3}$$

with $v = V - V^*$ being the deviation of the voltage from its steady-state value and $g_M = (\partial I_{mem}/\partial V)^*$ is the slope of the *instantaneous* $I - V$ curve . The time-dependent

variables

$$w_k \;=\; (x_k - x_k^*) \,/\, \left(\frac{dx_{k,\infty}}{dV}\right)^* \quad \text{for } k = 1, \cdots, N \tag{4}$$

are proportional to the deviation of the activation or inactivation variables x_k from their steady-state values $x_k^* = x_{k,\infty}(V^*)$ and are expressed in units of mV. The time constants τ_k correspond to those of the activation and inactivation variables evaluated at V^* and the parameters

$$g_k \;=\; \left(\frac{\partial I_{mem}}{\partial x_k}\right)^* \left(\frac{dx_{k,\infty}}{dV}\right)^*, \tag{5}$$

written in units of conductance, measure the strength of the effect that the variable x_k has on the voltage. Note that in the linear approximation, the dynamical variables w_k are no longer multiplied by a voltage-dependent term as they were in the original conductance-based description.

Activation or inactivation variables can be classified according to the sign of their corresponding parameter g_k. Examples of variables with $g_k < 0$ are the activation variables of Na^+ and Ca^{2+} currents and inactivation variables of K^+ currents. Examples of variables with $g_k > 0$ include inactivation variables of Na^+, Ca^{2+} currents, activation variables of K^+ currents and the activation variable of the H current. For $g_k > 0$ the corresponding variable opposes voltage change (negative feedback), while $g_k < 0$ indicates that the variable amplifies voltage change (positive feedback). Previous modeling studies (reviewed in Hutcheon and Yarom 2000) have shown that a variable with $g_k > 0$ can create a subthreshold resonance (a *resonant* variable), whereas a variable with $g_k < 0$ can amplify an existing resonance (an *amplifying* variable).

Conductance-based models generally comprise many active ionic currents and are therefore described by a large number of activation or inactivation variables. Despite the simplification of linearity, such systems of equations can still be hard to handle analytically. However, it is often possible to reduce the number of variables to two or three, while still accurately modeling the behavior near the holding voltage. This can be achieved by considering that very fast variables (such as the activation variable of fast sodium channels) are instantaneous, by merging together variables with similar time constants, and by noting that very slow variables average over the voltage, to provide a steady current. The resulting equations have the same form as equation (3) but with effective values C and g for the capacitance and leak respectively. The effective leak g can be zero or even negative, while the resting potential remains stable. Examples of the linearization method are given in the Appendix for two conductance-based models, together with the further approximations leading to reductions in the number of variables to two or three.

Two-variable subthreshold dynamics. For the case of two variables the neuron is described by the two equations

$$C\frac{dv}{dt} \;=\; -gv - g_1 w + I_{app}(t)$$

$$\tau_1 \frac{dw}{dt} = v - w \tag{6}$$

with four parameters, C, g, g_1 and τ_1. However, expressing time in units of τ_1, and dividing the voltage equation (6) by C makes it apparent that the model only depends on two dimensionless parameters $\alpha = g\tau_1/C$ and $\beta = g_1\tau_1/C$. The quantities α and β parameterize the behavior of the neuron near V^*, and can be considered as representing a point on a plane. α represents an effective leak, while β represents an effective coupling between the two variables. β measures the influence of the w variable on the membrane potential.

Three-variable subthreshold dynamics. The analysis is also extended to include a third variable. The subthreshold dynamics is then described by

$$\begin{aligned} C\frac{dv}{dt} &= -gv - g_1 w_1 - g_2 w_2 + I_{app} \\ \tau_1 \frac{dw_1}{dt} &= v - w_1 \\ \tau_2 \frac{dw_2}{dt} &= v - w_2 \end{aligned} \tag{7}$$

where in this paper a restriction is made to $g > 0$. Four independent and dimensionless parameters g_1/g, g_2/g, $\tau_1 g/C$ and $\tau_2 g/C$ are now needed to fully describe the model.

Models of Spiking Neurons

One of the major goals of the present paper is to investigate the effect of subthreshold resonance on the dynamics of spike emission. To this end, a simple spiking neuron model that exhibits subthreshold resonance, the *generalized integrate-and-fire neuron*, is introduced. To demonstrate that the general results derived for this simplified model carry over to more realistic neurons, two representative conductance-based models that are known from the literature to produce subthreshold resonance are also examined (*model I* and *model II*). In an attempt to cover the range of possible behaviors, the models are chosen to have different resonance mechanisms (hyperpolarization or depolarization activated currents) and also different resonant frequencies (near 10Hz and 50Hz respectively).

Generalized integrate-and-fire neuron (GIF). The integrate-and-fire (IF) model neuron provides a powerful tool for the understanding of neurons with passive membrane properties, and is the standard component of large numerical simulations of recurrent networks. However, its passive subthreshold behavior cannot capture the phenomenon of resonance. An extension of the IF model, which captures the subthreshold behavior of the two-variable model with a simple spike mechanism, is therefore the first spiking neuron model to be introduced here. The generalized integrate-and-fire (GIF) neuron is obtained by supplementing equations (3) with a threshold for spike generation at $v = v_\theta$, followed by a reset of the membrane voltage at $v = v_r$ (the auxiliary variables w_k considered here

have a slower dynamics than the spike, and therefore it is not appropriate to reset them also). In the case $g_k = 0$ for all k, the voltage equation reduces to the integrate-and-fire (IF) model. With two variables, this model is similar to a model recently proposed by Izhikevich (2001). The two-variable GIF model subject to an applied current is described by equation (6) where the parameters C, g, g_1 and τ_1 are kept fixed for the whole of the subthreshold regime. I_{syn} is the modeled synaptic current and $I_{app}(t)$ represents the applied current, to be described below. In this paper the threshold is chosen to be at -50mV, the rest (in absence of any input currents) at -70mV and the reset at -56mV. Because v measures the deviation from rest $v = V - V_{rest}$, this corresponds to $v_\theta = 20$mV and $v_r = 14$mV.

Conductance-based neurons.

Model I. A neuron with I_{Na}, I_K and I_H currents. The first model comprises a hyperpolarization-activated mixed cation current I_H and the Hodgkin-Huxley spike-generating currents. The form of the I_H current is taken from Spain et al. (1987) and comprises both fast f and slow s activation variables. The timescales of the two components are $\tau_f = 38$ms and $\tau_s = 319$ms and, as in Spain et al. (1987), taken to be voltage independent. The fast component has the greater contribution and determines the resonant frequency f_R, which is near 10Hz at physiological temperatures. A detailed model description can be found in the Appendix.

Model II. A neuron with I_{Na}, I_K, I_{NaP} and I_{Ks} currents. In contrast to the I_H model defined above, the second model neuron features two depolarization-activated currents: the slow potassium current I_{Ks} and the persistent sodium current I_{NaP}. In the language of Hutcheon and Yarom (2000) the I_{Ks} current generates the resonance and the I_{NaP} current amplifies its effect. A non-inactivating form (Gutfreund et al. 1995) is used for the I_{Ks} with an activation time-scale of $\tau_q = 6$ms (Wang 1993) giving a subthreshold resonance that is strongest at resonant frequencies around $35 - 55$Hz. Neurons with a resonance frequency or subthreshold-oscillations at about 40Hz are widespread (Puil et al. 1986; Pike et al. 2000) and the underlying mechanism is thought to sometimes involve the I_{Ks} and I_{NaP} currents (Llinás et al. 1991). Again, full details of this model are given in the Appendix.

Modeling the noisy synaptic input.

The massive synaptic bombardment received by neurons *in-vivo* represents a strong source of noise. Destexhe et al. (2001) provided evidence that an appropriate model of such a synaptic input is given by a fluctuating conductance with short correlation times related to the shapes of typical excitatory and inhibitory post-synaptic potentials. Hence, for the analysis of the firing rates of the two conductance-based models I and II the noise is modeled as in Destexhe et al. (2001) by the equations

$$\begin{aligned} I_{syn} &= g_e(t)(V - E_e) + g_i(t)(V - E_i) \\ \tau_e \frac{dg_e}{dt} &= g_{eo} - g_e(t) + \sigma_e \sqrt{2\tau_e}\xi_e(t) \end{aligned} \tag{8}$$

$$\tau_i \frac{dg_i}{dt} = g_{io} - g_i(t) + \sigma_i \sqrt{2\tau_i}\xi_i(t)$$

where ξ_e, ξ_i are delta-correlated Gaussian white noise terms. Representative values of the correlation times $\tau_e = 3$ms and $\tau_i = 10$ms are used here. The reversal potentials are taken to be $E_e = 0$mV and $E_i = -75$mV. The average conductances g_{eo}, g_{io} and the noise amplitudes σ_e and σ_i can be varied to explore a range of input conditions.

Modeling noise for the GIF neuron: In order to have a simple model with a membrane-potential-independent subthreshold resonance the synaptic inputs are modeled by a current comprising a direct drive I_0 and a white-noise source

$$I_{syn} = I_0 + I_N \sqrt{\tau_N}\xi(t) \tag{9}$$

where $\xi(t)$ is the delta-correlated Gaussian white-noise term with unit variance and I_N is the measure of the noise strength in nA. The factor τ_N is introduced to preserve units, and throughout this paper it is arbitrarily fixed at $\tau_N = 1$ms without affecting the generality of the results. The noise strength I_N can be related to a more intuitive measure: the standard deviation of the membrane voltage (in the absence of the spiking mechanism). In the two-variable GIF model, the standard deviation of the voltage σ_V takes the form

$$\sigma_V = I_N \sqrt{\frac{(C + g\tau_1 + g_1\tau_1)\tau_N}{2C(g + g_1)(g\tau_1 + C)}}. \tag{10}$$

Response of the neuron to an oscillatory drive

Subthreshold response. To characterize the subthreshold response, an oscillating current of frequency f is used. The applied current and resulting voltage response to this current are given by

$$\begin{aligned} I_{app} &= I_0 + I_1 \sin(2\pi f t) \\ V &= V^* + V_1(f) \sin(2\pi f t + \theta(f)) \end{aligned} \tag{11}$$

where both the phase difference $\theta(f)$ and the magnitude of the impedance

$$|Z(f)| = V_1(f)/I_1 \tag{12}$$

are functions of the driving frequency f. The existence of a peak in the $|Z(f)|$ versus frequency curve provides the definition of subthreshold resonance. The impedance $Z(f)$ can also be measured experimentally using a ZAP current (Puil et al. 1986).

Firing-rate response. In the context of examining the interactions between membrane frequency preference (resonance) and network oscillations, it is of interest to examine how the instantaneous firing rate of a neuron responds to a sine-wave modulation in the background of a noisy synaptic current

$$I_{app} = I_1 \sin(2\pi f t).$$

A regime is considered where the noisy synaptic drive is sufficiently strong to cause the neuron to fire stochastically, at an average rate r_0. The weak sinusoidal component then causes a weak modulation of the firing rate that will be apparent over many trials, see Figure 1. This quantity can also be thought of as the firing rate, averaged over a population of neurons each individually receiving a noisy drive, but responding collectively to the same weak oscillatory component present in the firing rates of presynaptic neurons. The form of this population, or trial-averaged instantaneous rate is

$$r = r_0 + r_1(f)\sin(2\pi f t + \phi(f)). \tag{13}$$

The analogy with the subthreshold voltage form in equation (11) is clear. Similarly, the response $r_1(f)$ is proportional to the strength of the modulatory current, leading to the introduction of the following quantity that measures the ability of a neuron to amplify a particular frequency

$$|A(f)| = r_1(f)/I_1 \tag{14}$$

called the *signal gain*, see for example Gerstner (2000). In the same way that a peak in the impedance $|Z(f)|$ quantifies subthreshold resonance, the existence and position of the peak in the quantity $|A(f)|$ will be the corresponding firing-rate measure of resonance.

Experimental studies have used either large amplitude sine-wave currents (Hutcheon et al. 1996b) or small-amplitude sine-wave currents when the voltage is very close to threshold (Pike et al. 2000). In both of these studies a strong effect was measured in the time-averaged rate itself and not in its modulation. The situation considered here is of weak oscillatory input leading to a linear response of the firing rate (higher-order harmonics are negligibly small). In this case the signal gain is a more sensitive measure of the frequency dependence of spike emission than the time-averaged firing rate.

Analytical methods. The firing-rate response of the GIF neuron can be computed analytically in the limit of large τ_1. Methods are sketched in the Appendix. Details will be published elsewhere (Brunel, Hakim and Richardson, in preparation).

Numerical methods. The numerical analysis of the firing-rate response of the GIF and conductance-based models was performed using a stochastic second-order Runge-Kutta algorithm (Honeycutt 1992), with a time step of 10μs and 20μs respectively. The amplitude of the modulatory current I_1 used in numerical measurements of the signal gain was varied until it was sufficiently small such that higher order non-linear effects were negligible. The length of simulation time needed to get accurate measurements for each frequency point varied between $1,000$ and $50,000$ seconds, depending on the firing rate and the particular level of noise chosen in the input current. To estimate the firing rate modulation at a given frequency, the instantaneous firing rate is computed in bins of 1 ms. The resulting histogram, sketched in figure 1, is then fitted by a sinusoid with a frequency equal to that of the oscillatory input current.

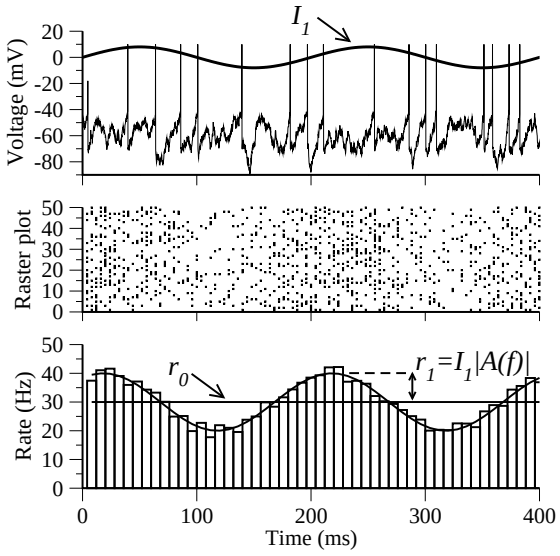

Figure 1: The response of the instantaneous firing rate to a weak sinusoidal input. The oscillatory current is applied on top of a noisy input that itself elicits firing at an average rate r_0 (see top panel). By averaging over many realizations (shown in the raster plot) the modulation of the instantaneous firing rate can be computed, and the characteristics (amplitude and phase) of the induced sinusoidal component of the firing rate obtained (lower panel). A bin width of 8ms was used for illustrative purposes in this figure.

RESULTS

Subthreshold properties of the membrane potential

The different classes of behavior in the subthreshold regime are examined first. Two and three-variable models, with parameters directly related to measurable membrane properties, are used to classify the different types of response to standard test currents. It is shown that the types of behavior that the neuron can exhibit at different holding voltages can be conveniently presented in graphical form for both the two and three-variable descriptions. The results are illustrated by two conductance-based models of spiking resonant neurons.

Subthreshold behavior of the two-variable model

The subthreshold behavior of the two-variable model is first classified with respect to stability and the response to standard test currents. Because the two-variable model is related to an underlying conductance-based description near a holding voltage V^*, it is parameterized by an effective leak $\alpha = g\tau_1/C$ and an effective coupling between the two variables $\beta = g_1\tau_1/C$. The parameters α and β can be used to represent the behavior of the neuron by a string of points on a plane, as the neuron is depolarized or hyperpolarized by an injected current. The borders separating different types of behavior are obtained through the analysis of equations (6), presented in detail in the Appendix.

Stability. The classification of the subthreshold regime starts with the determination of the parameter region where the neuron remains stable at the holding potential (without e.g. subthreshold oscillations or spike emission). Analysis of the stability of the membrane potential of the two-variable model determines an unstable region shown in brown in Figure 2. The region is bounded on one side by the vertical dashed line that signals the onset of spontaneous oscillations. On the other side, it is bounded by a diagonal line that corresponds to the total input conductance becoming zero, which can lead to spike emission. The rest of the analysis will focus on the stable region to the right of these two lines.

Response to oscillating current. The first experimental measure of subthreshold properties considered here is the voltage response to an oscillating input current. The magnitude and phase of this response measure the impedance of the neuronal membrane. A subthreshold resonance, signaled by the existence of peak in $|Z(f)|$ at some non-zero frequency f_R, occurs in the whole of the green region of Figure 2A (Hutcheon et al. 1996a). The line which bounds the region of the phase diagram in which resonance occurs starts at the point $\alpha = -1$, $\beta = 1$ (the intersection between the two instability lines) and for large α it tends towards the axis $\beta = 0$. Thus, in most of the stable region with $\beta > 0$ resonant behavior occurs. Positivity of β implies that the associated activation or inactivation variable is a resonant variable (Hutcheon and Yarom 2000).

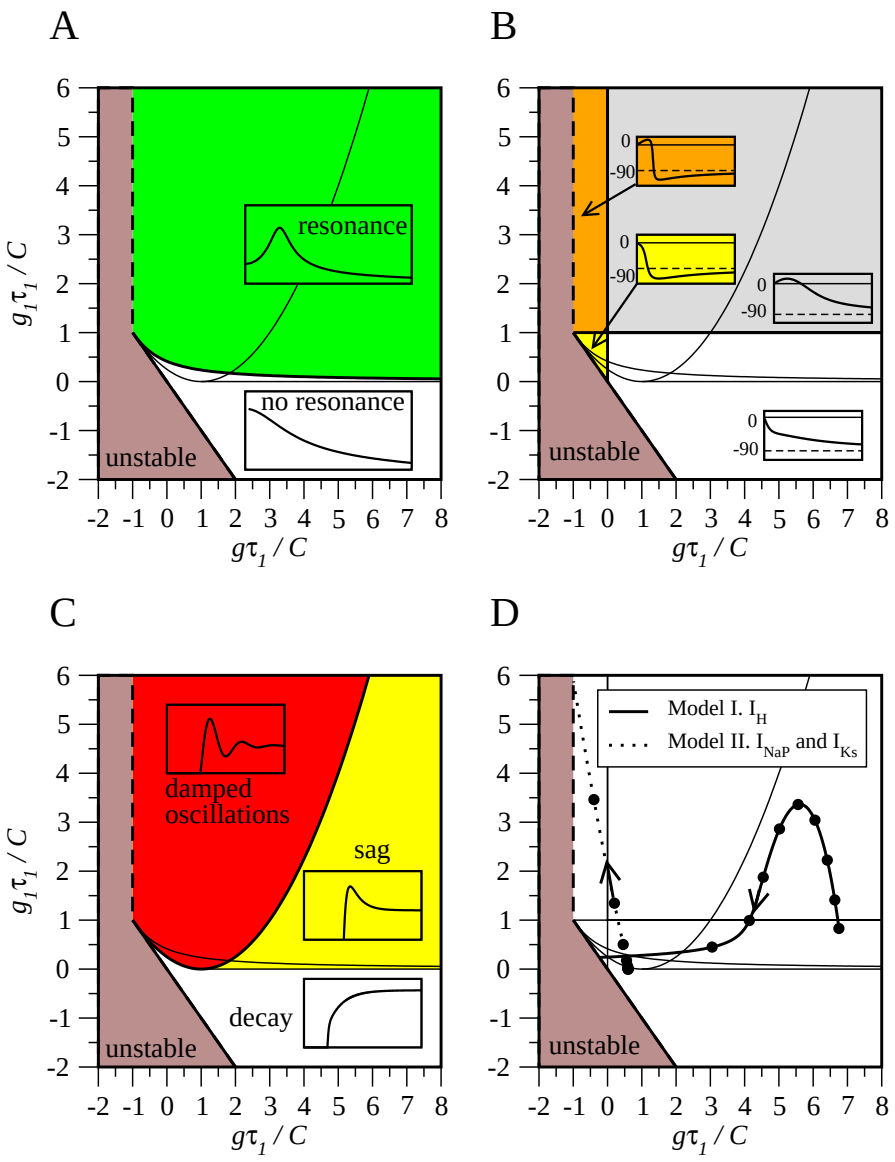

Figure 2: The subthreshold behavior of two-variable models. Brown marks the unstable region. The insets indicate qualitatively the response to the relevant test current, in regions in the space of parameters $\alpha = g\tau_1/C$ (the effective leak) and $\beta = g_1\tau_1/C$ (the effective coupling between the two variables) . (A) oscillating current injection, amplitude of the impedance. (B) phase of the impedance. (C) response to a square-pulse current. (D) trajectories of the two conductance-based model neurons in parameter space as their holding potential is increased. Model I (full line): $g_1 = g_f$ (see text and appendix) parameterizes the effect of the fast component of the current I_H on the voltage. The trajectory covers the range from -100mV to -56.5mV at which point the resting state is unstable and spikes are emitted. Model II (dotted line): $g_1 = g_q$ (see text and appendix) parameterizes the effect of the slow-potassium current I_{Ks} on the voltage. The trajectory covers the range -100mV to -57mV at which point spontaneous oscillations occur. In both cases the black points are at 5mV intervals, with the last point plotted before destabilization occurring at -60mV, and the arrows represent the direction of depolarizing membrane potential.

Phase response to oscillating current. Another quantity of interest is the existence of a zero phase-lag in the membrane potential response at non-zero frequency, seen in cortical neurons (Gutfreund et al. 1995). Analysis of the phase difference $\theta(f)$ between the oscillating current and the voltage response, defined in equation (11), shows that a zero phase-lag exists for $\beta > 1$. This quantity also coincides with the existence of a maximum in the phase and a phase advance from the driving current. A second line $\alpha < 0$ signifies the existence of a minimum in the phase, implying that at some frequencies the phase lag is greater that 90 degrees. Taken together, these criteria divide the phase diagram into four regions, plotted in Figure 2B. It should be noted that none of the lines separating the different qualitative responses of the phase correspond exactly to the presence of a resonance in the amplitude of the impedance.

Response to a square-pulse current. The application of a small step change in applied current provides a different assessment of subthreshold membrane properties. The response of the neuron to such current can be obtained explicitly (see the Appendix for details). At the level of the two-variable description the neuron can exhibit three different types of response to the square-pulse current shown, the voltage-time profiles of which are shown in the insets of Figure 2C:

(i) Damped oscillations. The neuron exhibits damped oscillations at frequency f_0 as it approaches its new holding membrane potential, when β is sufficiently large compared to α (the red region shown in Figure 2C).

(ii) Overshoot or sag. When $\alpha > 1$ and $\beta > 0$, but below the red region, the voltage time-course has a single overshoot (or sag if the current pulse is hyperpolarizing). This corresponds to the yellow region of figure 2C.

(iii) Passive decay. In all other areas of parameter space (the white region) the voltage changes monotonically from its initial to final resting voltage.

It is clear from panels A and C of Figure 2 that subthreshold resonance and damped oscillations are not equivalent. This fact, which was implicit in experimental measures of the resonant and natural frequencies (Puil et al. 1986), is often overlooked. An examination of Figure 2 shows that neurons can have damped oscillations but no resonance, and vice-versa. In fact none of the other measurements (the phase or response to a square-pulse current) of the neuron examined here give complete information about the existence of a resonance. However, close to the instability line, where the neuron is almost spontaneously oscillating, both resonance and damped oscillations are guaranteed to occur together.

Subthreshold behavior of the two conductance-based models

The diagram introduced in Figure 2 allows a visualization of the trajectory of the neuron through the space of parameters $\alpha(V^*)$ and $\beta(V^*)$ as the holding voltage V^* is varied. This is shown for the two model neurons defined in Methods and detailed in the Appendix.

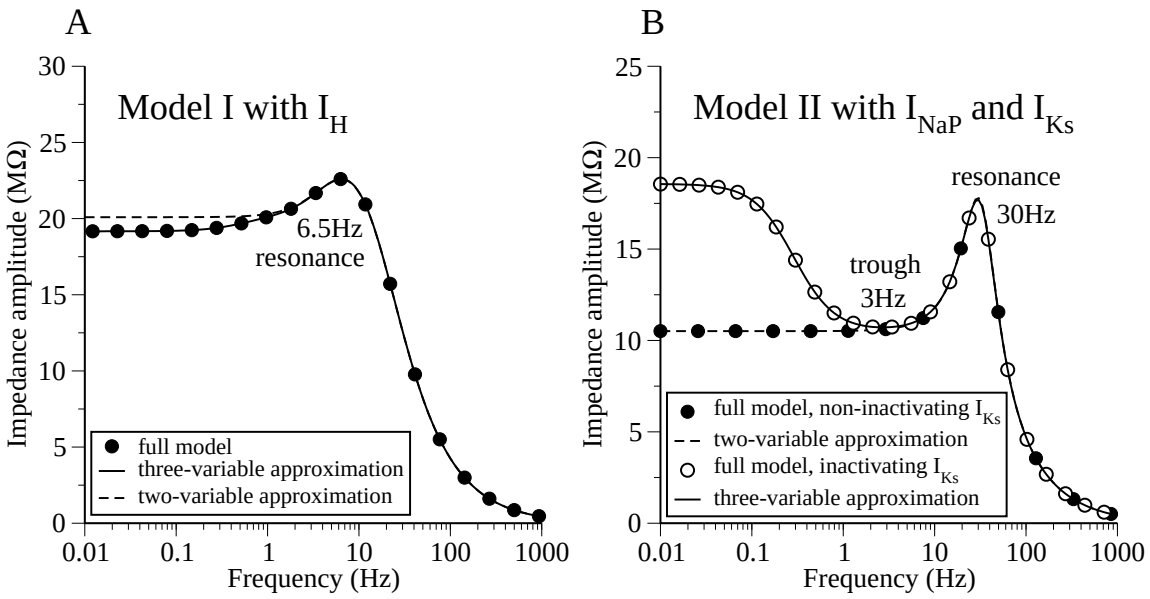

Figure 3: The frequency-dependent input impedance for the two model neurons held at -65mV, showing the level of approximation between the full ($\bullet$ and $\circ$ symbols), three-variable (bold lines) and two-variable (dashed lines) descriptions. (A) Model I. The three-variable model is obtained by taking the spike-generating currents to be instantaneous. The full and three-variable models agree closely for all frequencies plotted. The two-variable approximation is obtained by noting that the slow variable of the I_H current averages to a steady value for frequencies greater than about 2Hz. (B) Model II. The full non-inactivating I_{Ks} model ($\bullet$ symbols) and its two-variable approximation, obtained by taking the spike-generating currents to be fast. If an inactivation variable is included in the definition of the I_{Ks} current, an impedance profile ($\circ$ symbols) with a trough at 3Hz as well as a resonance at 30Hz is seen (see subsection *The three-variable model* and the Appendix for details). The corresponding three-variable model obtained by taking the spike-generating currents to be fast, but retaining the activation and inactivation variables of the I_{Ks} current, provides a good approximation of the full model.

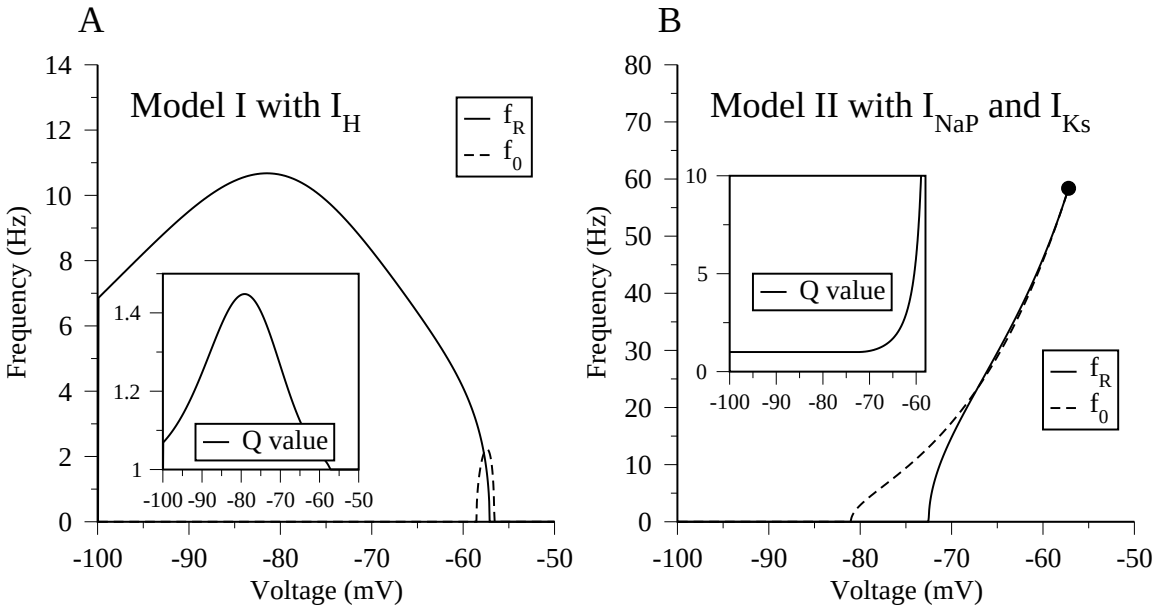

Figure 4: The resonance frequency f_R (bold line) and frequency of damped-oscillations f_0 (dashed line) of the two model neurons as a function of holding voltage. The corresponding Q values are also given which, following convention, measure the relative strength of the resonant peak $Q = |Z(f_R)|/|Z(0)|$. (A) Model I. A resonance exists for most of the subthreshold regime, whereas damped oscillations occur only in a narrow voltage range near the firing threshold (at -56.4mV). The resonance is strongest at -80mV with $f_R = 10$Hz. (B) Model II. In this case both resonance and damped oscillations exist above -72.5mV. The resonance strength increases as the membrane potential approaches the onset of spontaneous oscillations (indicated by the black circle at -57.2mV), above which the neuron fires periodically. The regions in which damped oscillations and resonance exist shown in these graphs can be compared with the trajectories in Figure 2D.

As the trajectory crosses different boundaries, so the neuronal response to input current will change qualitatively. The trajectories of the two model neurons, as parameterized by the changing effective leak g and coupling variable $g_1 = g_f$ or $g_1 = g_q$, are plotted in Figure 2D.

Model I. A neuron with I_{Na}, I_K and I_H currents. The resonance curve of the neuron is plotted in Figure 3A for a holding potential of -65 mV. The spike-generating currents are much faster than other timescales in the system and can be taken as instantaneous, reducing the full model to a three-variable description: the membrane potential and the two activation variables of the H current (see the Appendix for details). The impedance curve of the reduced three variable description is also shown in Figure 3A. Comparison with the full model shows that this reduction is extremely accurate. A further approximation, that the slow variable of the I_H current averages to a steady value, provides the two-variable description. The behavior of the neuron is therefore classified by its leak conductance g and the effect of the I_H fast variable f, through the two dimensionless parameters $\alpha = g\tau_f/C$ and $\beta = g_f\tau_f/C$. This two-variable description provides an excellent approximation of the original model for driving frequencies greater than 2Hz, as shown in Figure 3A. At frequencies greater than 2 Hz, the dynamics of the slow variable of the H current is too slow to follow the voltage changes and therefore to affect the resonance curve.

The effective leak α and effective coupling between voltage and H current β are calculated for a subthreshold voltage range of -100mV to -56.5mV using the linearization procedure. The corresponding trajectory is shown in Figure 2D and the resonance and damped oscillation frequencies are shown in Figure 4A. As can be seen, Model I exhibits a strong resonance at hyperpolarized values in the absence of damped oscillations (except in a narrow range between -58.5mV and -56.6mV near the firing threshold). This illustrates again that resonance and damped oscillations are distinct phenomena: oscillating and step currents probe different membrane properties. The Q-value, defined as $|Z(f_R)|/|Z(0)|$ (Hutcheon et al. 1996b), gives a measure of the strength of the resonance. As can be seen in Figure 4A, the I_H current provides the strongest resonance of $f_R \simeq 10$Hz at a holding voltage of -80mV. The trajectory also shows that the neuron responds with a sag/rebound to a step-current pulse: a well-known characteristic of the I_H current (Dickson et al. 2000). As the holding voltage is increased to more depolarized values the I_H current weakens until the resonance vanishes at around -57mV.

Model II. A neuron with I_{Na}, I_K, I_{Ks} and I_{NaP} currents. In a similar way to the previous case, the full conductance-based model can be reduced to a two-variable description by noting that the spike-generating currents are fast. This approximation is very accurate, as can be seen in Figure 3B (the non-inactivating I_{Ks} and two-variable profiles). The behavior of this neuron is classified by its leak g, the I_{Ks} coupling variable g_q and its time constant τ_q through the dimensionless parameters $\alpha = g\tau_q/C$ and $\beta = g_q\tau_q/C$. These quantities are calculated for a subthreshold voltage range of -100mV to -57mV, and the corresponding trajectory is plotted in Figure 2D. In distinction to Model I, the resonance here is driven by depolarization-activated currents. This can be seen in the

vertical-moving trajectory and the increasing Q value as the line of onset of spontaneous oscillations is approached. This neuron features both a resonant current in the activation of I_{Ks} as well as an amplifying current I_{NaP}. The amplification effect is clearly seen in a comparison of the Q values of the resonance of Model II with Model I (which lacks an amplifying mechanism). An examination of Figure 4B shows that the resonant frequency steadily increases as the line of onset of spontaneous oscillations is approached, a feature reminiscent of the "broad-frequency cells" in Llinás et al. (1991) which were also shown to feature a TTX-sensitive persistent sodium current as well as a delayed rectifier. The amplification is due to the fact that the I_{NaP} current *decreases* the effective leak (since the current amplifies voltage changes). Hence, the parameter α decreases as an effect of the activation of this current, and correspondingly the model moves towards the left in the diagram of figure 2D, in the direction of the line where spontaneous oscillations occur. On this line the Q value diverges.

Subthreshold behavior of the three-variable model

Though two-variable models capture the properties of a broad class of neurons, Figure 2A shows that they only provide two classes of impedance curves, either monotonously decreasing with increasing frequency (non-resonant case shown in white), or with a single peak at a preferred frequency (resonance case shown in green). Therefore, more complex impedance curves cannot be described with only two variables. For this reason, the same classification described above was performed for a model with three variables, defined in equations (7). The model is now specified by four parameters: the conductance ratios g_1/g and g_2/g, and the time constants τ_1 and τ_2 of the variables w_1 and w_2. Without loss of generality, the time constant of w_2 was chosen to be the faster variable, thus $\tau_2 < \tau_1$. When the faster variable is taken to be instantaneous, $\tau_2 = 0$, the model becomes equivalent to the two-variable model with $\alpha = (g + g_2)\tau_1/C$ and $\beta = g_1\tau_1/C$.

The classification of the three-variable model was done in terms of the presence or absence of damped oscillatory behavior in response to transient inputs, and presence or absence of resonant behavior as defined by the peaks of the impedance profile. Figure 5 shows the different regions of interest in the (g_1/g) versus (g_2/g) plane for several values of the times constants τ_1 and τ_2 relative to the time constant $\tau = C/g$.

Stability. As in the two-variable case, the equilibrium voltage may destabilize in two different ways: either the total conductance $g_1 + g_2 + g$ becomes negative (on the full black line of the four panels of figure 5), or spontaneous oscillations appear (on the dashed line of the four panels of figure 5). These two lines intersect at the point where the frequency of the spontaneous oscillations becomes zero. When the time constants are such that $\tau_2 \ll \tau_1$ the line where spontaneous oscillations arise becomes vertical. Thus, as stated above, in the limit $\tau_2 = 0$, the behavior of the two-variable model is recovered (compare Figure 5B with Figure 2).

Resonance and damped oscillations. Again, similar but distinct regions are observed

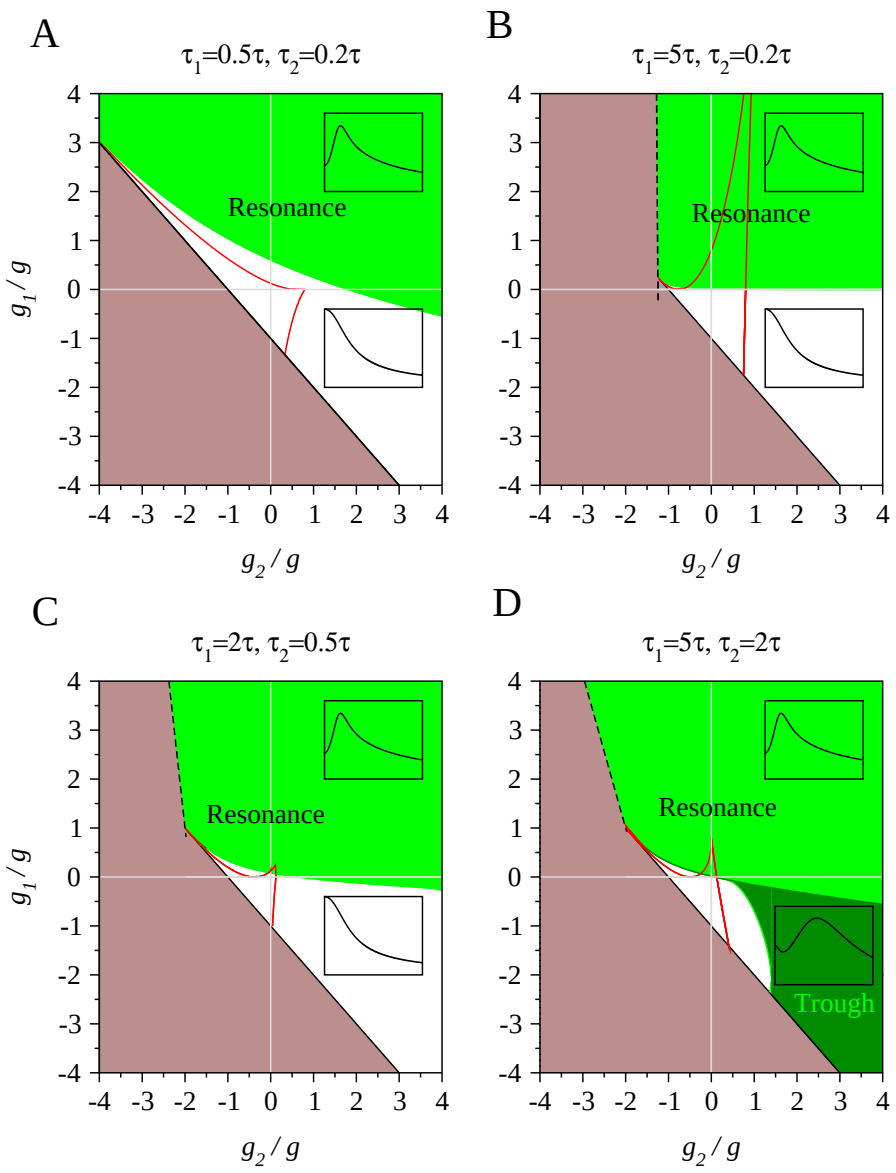

Figure 5: Phase diagram of the three variable model in the plane g_1/g, g_2/g, for different values of the time constants τ_1 and τ_2 relative to $\tau = C/g$ (marked above each panel). Unstable region is in brown. Green regions are regions where resonance occur. Dark green region in lower right panel **D**: resonance with a trough at a lower frequency. The red lines indicate the boundaries of the regions in which damped oscillations occur in response to a current step. See text for more details.

in which damped oscillations and resonant behavior occur. In the upper-left quadrant of each panel (where the slower variable is 'resonant', $g_1 > 0$, while the faster variable is 'amplifying', $g_2 < 0$), both damped oscillations and resonant behavior are present in most of the stable region. In the upper-right quadrant where both variables are 'resonant', damped oscillations and resonant behavior are found almost throughout. In the lower-left quadrant, both variables are amplifying: the neuron exhibits neither damped oscillations nor resonance, and destabilizes exclusively by the total conductance becoming zero.

The appearance of a trough. In the bottom-right quadrant (where the slower variable is now 'amplifying' $g_1 < 0$ and the faster variable is 'resonant' $g_2 > 0$), a qualitatively new phenomenon is observed, depending on the values of the time constants. When the two variables τ_1 and τ_2 are slower than the time constant $\tau = C/g$ the amplitude of the impedance has a local minimum or trough, at a finite frequency (indicating a suppression of the membrane response at that frequency) followed by a resonant peak at higher frequency. One example of such subthreshold dynamics is a neuron with an inactivating potassium current with a relatively large activation time constant τ_2 and a much larger inactivation time constant τ_1 with overlapping steady-state activation and inactivation functions (a window current). In fact a model of the I_{Ks} current that also includes an inactivation variable (see Appendix for details) gives exactly this effect. The frequency-impedance curve for such a neuron is plotted in Figure 3B and shows a close similarity to the experimentally measured impedance curve of the fast-spiking interneurons measured in (Pike et al. 2000). A two and three-variable reduction of this full conductance-based model are also plotted for comparison. Another possibility would be to have the two variables implemented in two active persistent currents: a potassium current with activation time constant τ_2 and a sodium or a calcium current with slower activation time constant τ_1.

As expected, increasing the complexity of the model in terms of the number of descriptive variables also increases the range of neuronal behavior that can be modeled. In summary, a one-variable model (like the subthreshold dynamics of the leaky integrate-and-fire neuron) can have only a monotonously decaying impedance; a two-variable model can have either a monotonously decaying impedance, or an impedance with a resonant peak, whereas a three-variable model can describe the two above-mentioned behaviors, and in addition an impedance with a trough at low frequency followed by a peak at higher frequency.

The firing-rate resonance

In this section the effect of the subthreshold resonance on the dynamics of the firing rate is investigated. The aim of the analysis is to determine when a small oscillatory component in the synaptic inputs of a given neuron will be amplified in its output and how this depends on the subthreshold properties of the considered neuron.

The current used to model the synaptic bombardment such a neuron would experience

in vivo comprises a noisy hyperpolarizing or depolarizing drive as well as a weak sinusoidal component of frequency f. The signal gain $A(f)$ defined in equation (14) and illustrated in Figure 1 measures the strength of the temporal modulation of the instantaneous firing rate induced by the oscillating current. It is the firing-rate analog of the impedance $Z(f)$, and it is the existence of a peak in the signal gain that categorizes the amplification of frequencies in the outgoing spike train of resonant neurons. As will be shown, the noise inherent in biological networks is an important factor in determining the frequency that is maximally amplified.

The range of behavior is first examined by the use of a *generalized integrate-and-fire* (GIF) model neuron. These results are then illustrated by two conductance-based models with spike generating currents, and also (i) an I_H current, or (ii) I_{NaP} and I_{Ks} currents.

Firing-rate resonance in the GIF model neuron

In the previous section the subthreshold behavior of a general two-variable model was analyzed in detail. As described in Methods, a simple spike mechanism (threshold and reset) can be added to the two-variable description to produce a generalization of the integrate-and-fire neuron. This provides the simplest mathematical description of a spiking neuron with resonant subthreshold dynamics and allows a direct link to be made between the subthreshold characteristics and the statistical properties of the outgoing spike train. In spite of its simplicity, the GIF model provides a good approximation to more complete descriptions of neurons as will be seen in the next section.

The model examined here is parameterized by $C = 0.5$nF, $g = 0.025\mu$S, $g_1 = 0.025\mu$S and $\tau_1 = 100$ms, giving a subthreshold resonance frequency f_R near 5Hz. The signal gain $A(f)$ was examined as a function of frequency for different respective strengths of the constant I_0 and noisy I_N components of the injected current, defined in Methods equation (9). It should be noted that the sinusoidal component I_1 is always taken to be weak in the present work.

The fact that the neuron is induced to fire at a frequency r_0 by the applied current implies that there are now two distinct and independent frequency scales: the subthreshold resonant frequency f_R, controlled by the subthreshold dynamics of the membrane potential, and the background firing frequency r_0, which is controlled by the characteristics of the externally applied noisy current. It is useful to distinguish situations depending on whether r_0 is lower or greater than f_R.

High firing rate $r_0 > f_R$: When the firing rate of the neuron is greater than its resonance frequency, two distinct modes of behavior were identified; (i) when the neuron fires regularly due to a direct drive with a low noise term (*low noise*), and (ii) when the neuron fires irregularly due to a high noise term, and a weak direct drive (*high noise*). Histograms of the response of these two cases to a current composed of a non-oscillating interval, an interval with a component of frequency $f_R = 5$ Hz and a final interval with a component of frequency $r_0 = 20$ Hz are plotted in Figures 6A and 6B. The full frequency-dependent

profiles of the signal gain $A(f)$ and phase $\phi(f)$ are also given in the lower two panels, Figure 6C and 6D.

(i) *Low noise.* The neuron fires regularly under the action of a strong direct drive $I_0 =$ 0.95nA perturbed by a weak noise term $I_N = 0.11$nA (σ_V=0.68mV). In this regime (the red curves of Figure 6) the neuron behaves as a non-linear oscillator of frequency r_0. In the spike histogram (Figure 6A) it is clear that the modulation is strongest in the third interval where the modulation of the current is at a frequency of 20Hz, equivalent to the firing rate.

(ii) *High noise.* In the converse case of noise-driven irregular firing (still at an average rate of $r_0 = 20$Hz) with $I_0 = 0.78$nA and $I_N = 0.55$nA ($\sigma_V = 3.4$mV) the amplification properties of the resonant neuron change. As shown in the corresponding (blue) spike histogram of Figure 6B the amplification is now strongest in the second interval of the response, corresponding to a modulation of the input current at a frequency equal to the subthreshold resonance $f_R = 5$Hz. Note that the noise level chosen here corresponds to the typical magnitude of membrane potential fluctuations measured *in vivo*, which are around 3-5 mV(Destexhe and Paré 1999; Anderson et al. 2000).

It is instructive to examine the signal gain for different values of noise, whilst the firing rate r_0 is kept constant through compensatory changes of the direct drive I_0, see Figure 6C. As the relative strength of the noise is increased the signal-gain peak at the firing rate decreases and vanishes before the peak at the resonance frequency emerges at higher noise levels. The green curve in Figure 6C shows an intermediate case with a flat signal-gain profile. The curves showing the phase in Figure 6D show qualitatively similar behavior, except that the peaks (indicating the greatest phase advance) are at lower frequencies than the corresponding peaks in the signal gain.

Low firing rate $r_0 < f_R$. When the firing rate r_0 is lower than the resonant frequency f_R, the 'low noise' (regular firing) situation becomes almost impossible to reach, because in absence of noise the neuron often starts to fire at a finite frequency (a type II neuron, see e.g. Rinzel and Ermentrout 1989). In this case firing at low frequencies can only be achieved through the action of a noisy current, rendering neuronal firing irregular. Thus, in practice, low firing rates imply high noise (noise-driven firing). When $r_0 < f_R$, the inter-spike interval is sufficiently long such that the neuron has time to explore its subthreshold regime and begin to "resonate" before firing. As could be expected, the subthreshold resonant frequency is therefore strongly evident in the signal gain, see Figure 7A in which the neuron was driven by a weak direct current $I_0 = 0.50$nA and noise term $I_N = 0.55$nA ($\sigma_V = 3.4$mV). The full profile of the signal gain demonstrates that the frequency most preferentially amplified is the subthreshold resonance $f_R = 5$Hz, as in Figure 6B. This case is therefore similar to the high-firing-rate case (ii) for which noise also dominated the firing process, despite the fact that the inter-spike dynamics are quite different.

The amplitude and phase of the signal gain $A(f)$ give a full picture of the changing behavior as the neuron moves between regular firing and irregular noise-driven firing in these two cases. As stated previously, the advantage of the GIF neuron is that it

allows for a direct link between the subthreshold properties and their effect on the firing rate. A mathematical analysis, presented elsewhere (Brunel, Hakim and Richardson, in preparation), provides analytical expressions for the signal gain and its phase in terms of the parameters of the model, in the limit that τ_1 is long. The mathematically generated curves have been plotted in Figures 6C, 6D , 7A and 7B for comparison with data from numerical simulation. All signal-gain amplitude profiles are normalized to 1 at $f = 0$, see Appendix.

The results can be summarized by the following two statements: (i) When the noise is low and the firing regular, a resonant neuron preferentially amplifies input frequencies at the firing rate itself. (ii) In cases of irregular noise-driven firing a resonant neuron will preferentially amplify an input frequency close to its subthreshold resonance. It should be noted that the first mode (i) of amplification is not restricted to resonant neurons. In fact this type of behavior is also seen in passive neurons and has been demonstrated experimentally (Knight 1972). In this situation the neuron does not directly communicate any information about its subthreshold properties to the network. The second mode of amplification (ii), in which the preferential amplification is at a frequency *intrinsic* to the cell, is particular to resonant neurons: the mathematical analysis directly links this firing-rate resonance with the existence of a subthreshold resonance.

Conductance-based models

The analysis of a resonant GIF neuron above demonstrated that there are two distinct modes of behavior with respect to the amplification of particular frequencies. In the case of low noise, the frequency most strongly amplified was at the firing rate (a property also of passive neurons) whereas in the case of high noise the amplification was most strong at the intrinsic resonant frequency of the cell.

These results were obtained using the idealized GIF model in which the Hodgkin-Huxley action potential is replaced with a voltage threshold and reset. A further assumption is that the subthreshold behavior is the same at all holding voltages. Another simplification is that a current-based white noise term was used to model the synaptic bombardment, rather than a more realistic temporally correlated conductance-based noise. Given these approximations, it should be tested if the results of the previous section carry over to more complete models that include spike-generating and other voltage-dependent currents, together with conductance noise (Destexhe et al. 2001). The analysis above was therefore repeated for the two conductance-based model neurons that are described in Methods and the Appendix and for which the subthreshold resonance behaviors are depicted in Figures 3 and 4.

Model I. A neuron with I_H, I_{Na} and I_K currents. The amplitude of the signal gain was examined in both the low and high noise regimes analogous to that shown in Figures 6 and 7. As can be seen in Figure 4A the subthreshold resonance frequency varies with holding voltage. However, as seen in the Q values in the same figure, the dominating

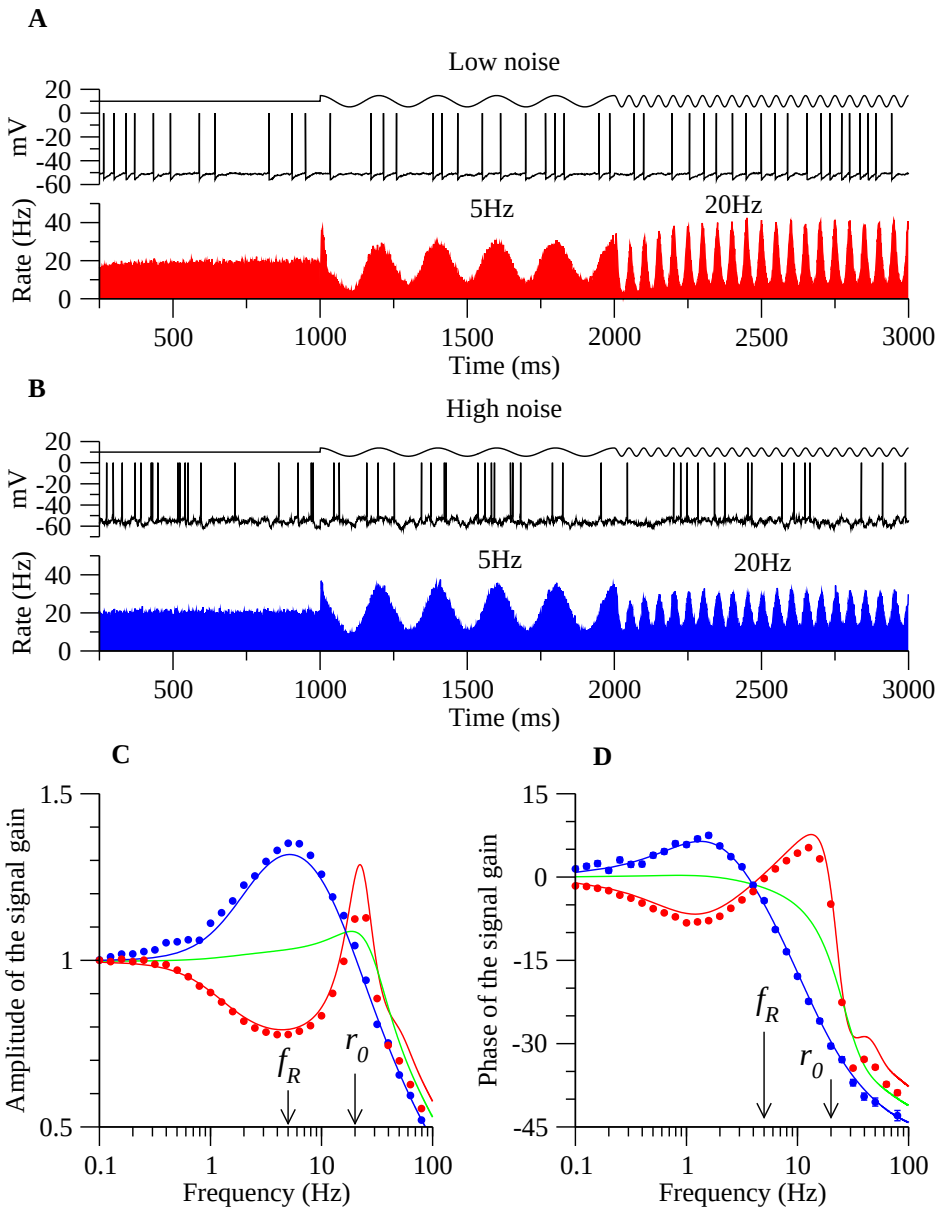

Figure 6: Effect of noise strength on the amplification of a frequency f in the firing rate of a resonant neuron. Two cases are considered: low noise (red) and high noise (blue). The particular GIF model neuron ($C = 0.5$nF, $g = 0.025\mu$S, $g_1 = 0.025\mu$S and $\tau_1 = 100$ms) has a resonance near 5Hz and in all cases the firing rate is kept at $r_0 = 20$Hz. Panels A and B; simulation of a three-second current injection protocol. $0-1$s: injected noisy current with no oscillatory component. $1-2$s: addition of a 5Hz (f_R) sinusoidal component. $2-3$s: sinusoidal component at 20Hz (r_0). (A) Low-noise case ($I_0 = 0.95$nA, $I_1 = 0.024$nA and $I_N = 0.11$nA) in which the neuron fires regularly. The amplification is greatest at $f = r_0 = 20$Hz. (B) High-noise case ($I_0 = 0.78$nA, $I_1 = 0.059$nA and $I_N = 0.55$nA). The strongest amplification is at the resonance frequency $f = f_R = 5$Hz. (C) Signal gain amplitude $|A(f)|$ versus frequency. (D) Phase of the signal gain $\phi(f)$ versus frequency. Both low (red curves) and high (blue curves) noise cases with the green curves representing an intermediate case ($I_0 = 0.92$nA and $I_N = 0.22$nA giving $\sigma_V = 1.36$mV). The signal gain curves are normalized to 1 at $f = 0$, see Appendix. The full lines are the theoretical predictions and the symbols come from numerical simulations of the model.

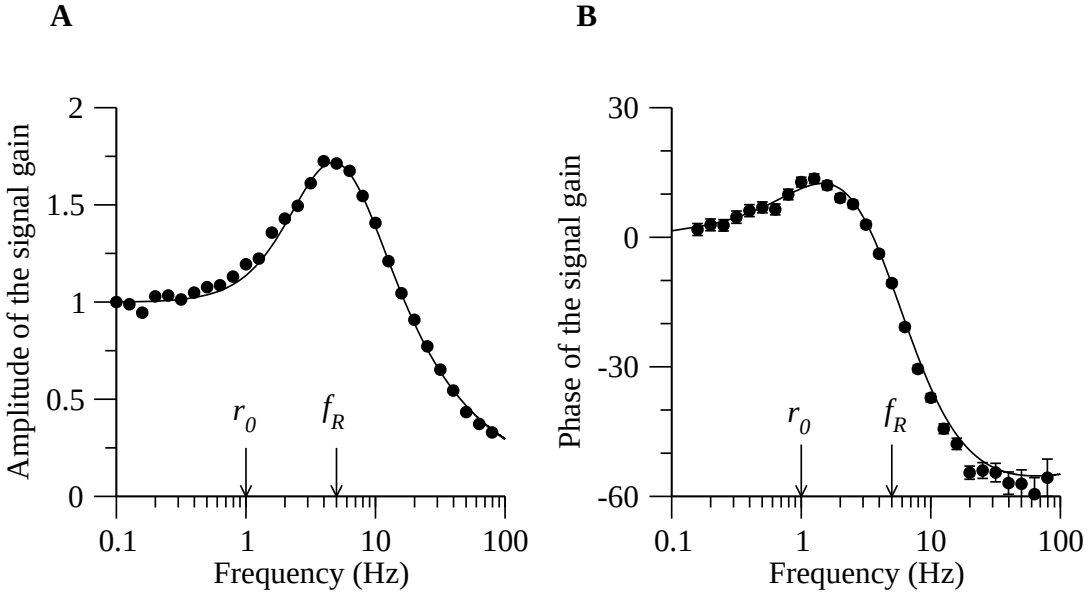

Figure 7: The signal gain for the case of noise-driven firing at a low rate. GIF model, same parameters as in Fig. 6. (A) The amplitude $|A(f)|$. The frequency most strongly amplified is at the subthreshold resonance of 5Hz. (B) The phase $\phi(f)$ of the signal gain. There is a phase advance at low frequencies as well as peak at around 2Hz. The signal gain curves have been normalized to pass through 1 at $f = 0$. The full lines are the theoretical predictions and the symbols come from numerical simulations of the model. The firing rate r_0 and the subthreshold resonance frequency f_R are shown by arrows.

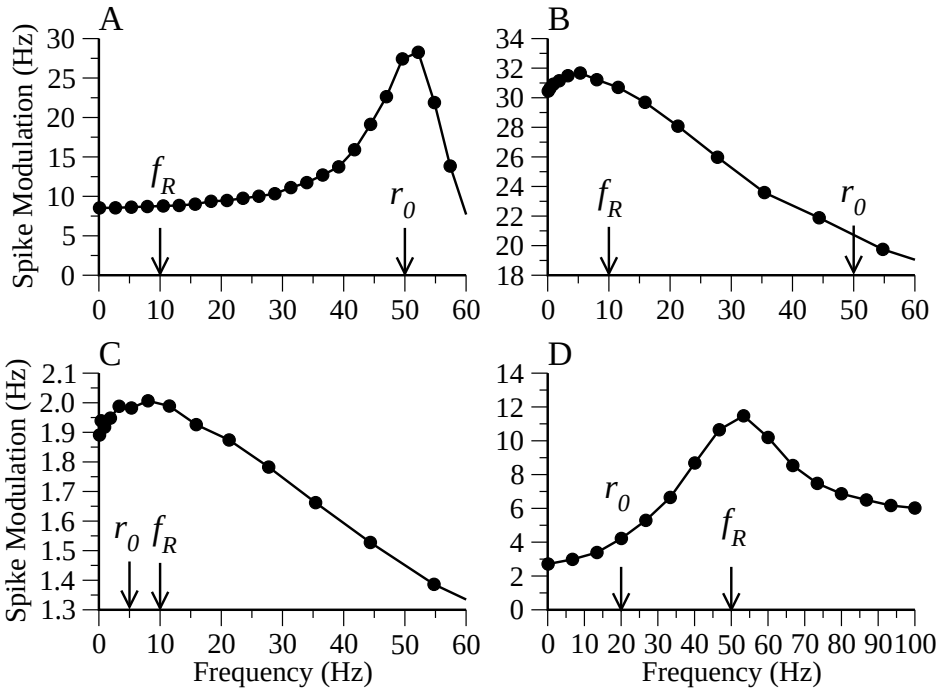

Figure 8: The spike-response ($I_1|A(f)|$) to a weak applied oscillating current (amplitude I_1) for regular and noise-driven firing modes for two conductance-based models of resonant neurons. (A) Model I: regular firing ($g_{eo} = 0.01\mu$S, $g_{io} = 0.0085\mu$S, $\sigma_e = \sigma_i = 0.0005\mu$S, $I_1 = 0.02$nA). The strongest amplification is at a frequency equal to the firing rate $r_0 =$ 50Hz. (B) Model I: noise-driven irregular firing at high rate ($g_{eo} = 0.01\mu$S, $g_{io} = 0.015\mu$S, $\sigma_e = \sigma_i = 0.01\mu$S, $I_1 = 0.2$nA). The strongest amplification is now near the resonant frequency $f_R = 10$Hz. (C) Model I: noise-driven firing at low rate $r_0 \sim 5.5$Hz ($g_{eo} =$ 0.01μS, $g_{io} = 0.063\mu$S, $\sigma_e = \sigma_i = 0.015\mu$S, $I_1 = 0.1$nA). Again the peak amplification is at the resonance frequency $f_R = 10$Hz. (D) Model II: noise-driven firing at low rate ($g_{eo} = 0.02\mu$S, $g_{io} = 0.012\mu$S, $\sigma_e = \sigma_i = 0.01\mu$S, $I_1 = 0.1$nA). The strongest amplification is near the resonant frequency of this neuron, at about 50Hz. The error bars are smaller than the symbol size.

resonance frequency f_R is near 10Hz.

Low noise with high firing rate $r_0 > f_R$. The synaptic drive was parameterized by the conductances $g_{eo} = 0.01\mu$S, $g_{io} = 0.0085\mu$S and noise strengths $\sigma_e = \sigma_o = 0.0005\mu$S eliciting regular firing at a rate r_0 close to 50Hz. As can be seen in Figure 8A, the signal gain peaks at this firing-rate frequency.

High noise with high firing rate $r_0 > f_R$. The synaptic drive was parameterized by the conductances $g_{eo} = 0.01\mu$S, $g_{io} = 0.015\mu$S and noise strengths $\sigma_e = \sigma_o = 0.01\mu$S also giving a firing rate r_0 close to 50Hz. As expected in this case of irregular firing, the peak in the signal gain (Figure 8B) is now at the resonant frequency $f_R = 10$Hz.

High noise and low firing rate $r_0 < f_R$. The synaptic drive was parameterized by the conductances $g_{eo} = 0.01\mu$S, $g_{io} = 0.063\mu$S and noise strengths $\sigma_e = \sigma_o = 0.015\mu$S giving a low (but noise-driven) firing rate of $r_0 \sim 5.5$Hz. As in the previous example of noise-driven firing, the peak in the signal gain is near the resonant frequency of 10Hz, Figure 8C.

Model II. A neuron with I_{KS}, I_{NaP}, I_{Na} and I_K currents. The Q values for this model (see Fig. 4B) demonstrate that the resonance is strong for a range of frequencies with a peak at the onset of spontaneous oscillations near 55Hz. As the subthreshold resonance is at relatively high frequencies, the only case examined for Model II is that for which the firing rate is less than the resonant frequency $r_0 < f_R$.

Noise-driven firing with $r_0 < f_R$. The synaptic drive was parameterized by the conductances $g_{eo} = 0.02\mu$S, $g_{io} = 0.012\mu$S and noise strengths $\sigma_e = \sigma_o = 0.01\mu$S inducing a firing rate of $r_0 \simeq 20$Hz. As can be seen in Figure 8D, the signal gain profile is peaked at $50 - 55$Hz: near the subthreshold resonance frequency.

The effect of the conductance increase from the synaptic drive. It should be noted that the conductance change caused by the modeled noise (see Eq. 8) has the effect of increasing the value of the subthreshold resonance frequency, relative to that which would be measured in the absence of synaptic drive. In Fig. 8, for the case of Model I (case of high noise and high firing rate) the conductance change corresponded to a 70% increase in the leak. This effect increased the subthreshold resonant frequency by about 1Hz over the voltage range -100mV to -60mV. For Model II (for which the conductance increase was 90%) the corresponding increase in the subthreshold resonant frequency was less than 2Hz. Larger synaptic conductances lead to larger shifts in the subthreshold preferred frequency, and consequently in the firing-rate preferred frequency as shown in Fig. 9 for the case of Model II. The preferred frequency is close to 50Hz for a conductance change of 100%, but increases to about 60Hz and 80Hz for a conductance change of 200% and 400% - values similar to some estimates of conductance changes *in vivo* (Destexhe and Paré 1999). The frequency where the spike rate is in phase with the input increases accordingly. The shift of the firing rate resonant frequency is related to the shift in subthreshold frequency. The latter shift can be calculated using equation (20) of the Appendix. The strength of subthreshold resonance decreases with an increase in synaptic

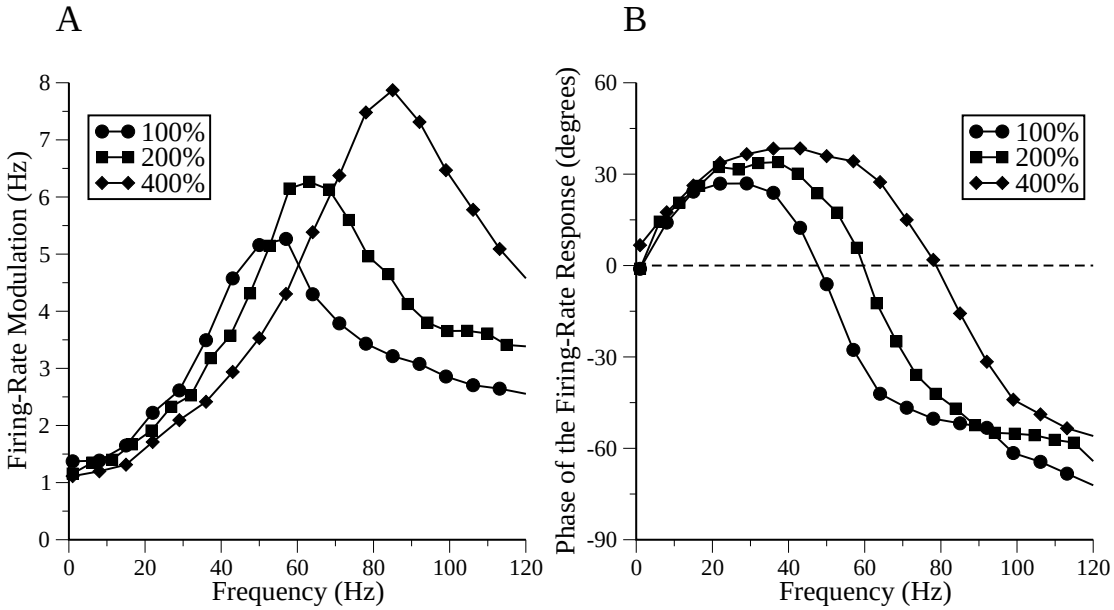

Figure 9: The effect of increasing synaptic conductance on the modulation and phase of the spike-response ($I_1|A(f)|$). Model II, for which $g_L = 0.037\mu$S, with synaptic-conductance input that increases this conductance by 100% (circles, $g_{e0} = 0.021\mu$S, $g_{i0} = 0.016\mu$S), 200% (squares, $g_{e0} = 0.038\mu$S, $g_{i0} = 0.036\mu$S) and 400% (diamonds, $g_{e0} = 0.076\mu$S, $g_{i0} = 0.072\mu$S). (A) spike rate modulation. The spike-rate resonant frequency is shifted to $\simeq$ 50Hz, 60Hz and 80Hz for conductance increases of 100%, 200% and 400% respectively. (B) phase. The frequency where the spike rate is in phase with the input has a corresponding shift to higher values. In all cases the amplitude of the sinusoidal current I_1 was 0.05nA and $\sigma_e = \sigma_i = 0.01\mu$S, eliciting a background firing rate of 20 Hz.

conductance, near a particular holding voltage. Thus, one would expect that the strength of the firing rate resonance would also decrease with the conductance increase. However, this is not necessarily the case, as shown in Fig. 9 where it is seen that the resonance strength increases with the conductance increase. The increase in this case appears to be due to the fact that the neuron spends more time at values of the membrane potential close to threshold, where the subthreshold resonance is stronger (see Fig. 4).

In summary, the conclusions drawn in the analysis of the GIF model neuron also hold for two distinct conductance-based models of resonance: the neurons amplify frequencies near their subthreshold resonance frequency under conditions of noise-driven irregular firing. A supplementary feature is that conductance-based synaptic noise increases the subthreshold resonance frequency. This in turn increases the frequency for which the firing rate is preferentially modulated, in the irregular firing regime.

DISCUSSION

Many classes of neurons throughout the nervous system exhibit subthreshold resonance. In this paper, we systematically studied the effect of this intrinsic frequency preference on both the subthreshold properties and the dynamics of the firing rate. Using reduced models as well as two example conductance-based model neurons, it was found that resonant neurons can amplify an oscillatory component in their input as they transmit it to post-synaptic targets. When the noise from the synaptic bombardment is significant, the frequency most strongly amplified is the subthreshold resonant frequency itself. The results of this study underline the importance of taking noise into account when examining neuronal response, and provides a first step in the understanding of the role of resonance in oscillations at the network level.

Subthreshold dynamics

Our analysis of two and three-variable neuronal models classifies a broad range of subthreshold behavior, providing a unifying framework in which different models can be inserted and compared. In particular, it shows that resonance and damped oscillations in response to transient inputs occur in overlapping but different regions of parameters.

Neurons can exhibit resonance when they include a sufficiently slow variable that opposes voltage change as previously emphasized (see e.g. Hutcheon and Yarom 2000). In this case, the negative feedback at low frequencies together with the suppressed response at high frequencies creates a band-pass filter which gives the resonant response but not a damped-oscillatory response. Figure 2 shows that having a sufficiently slow variable that opposes voltage change is indeed a sufficient condition for resonant behavior. It is however not a necessary condition since even a fast variable (i.e. $\tau_1 < C/g$) can produce resonance as long as its conductance g_1 is sufficiently large. In fact, an examination of

the regions in Figure 2 shows that resonant neurons with slow variables are generally non-oscillating, whereas those with fast variables are generally intrinsically oscillating. Conversely, neurons exhibiting damped oscillations do not necessarily have resonance if the damping of the oscillation is strong enough. This appears in a small parameter region where the effective coupling between the two variables is weak, as shown in Figure 2.

Our analysis also clarifies the relationship between the phase and the amplitude of the impedance. Phase advance of the membrane potential at low frequencies implies a peak in the impedance profile, but the reverse is not necessarily true, if the resonance is too weak.

Further analysis of three-variable models identified an impedance profile with a trough at low frequency, followed by a peak at higher frequencies. Such behavior was recently found experimentally in CA1 interneurons of the hippocampus by Pike et al. (2000). The criteria for a trough in the impedance profile are two active components that act on a slower time-scale than the membrane time constant. The slowest of the two variables must act to amplify voltage change, whereas the faster should act to oppose the change. An explicit example was given in terms of a neuron with an inactivating slow potassium current.

The analytical results presented can be used in the interpretation of experiment in two ways. They allow for the systematic building of a minimal model of a neuron, given the experimentally measured impedance profile. Firstly, the qualitative features of the resonance curve indicate the minimal number of variables needed (e.g. two variables for neurons with a single peak in the curve, three variables for neurons with a trough followed by a peak); secondly, the parameters of the model can be obtained quantitatively by fitting the impedance curve of the given model to the data. From an experimental point of view, they provide hints for the type of currents, or combination of currents, needed to achieve given resonance properties (see also Hutcheon and Yarom 2000).

The general subthreshold "phase diagrams" that were introduced here are related to several diagrams which appeared previously in the literature for particular neurons. In models with persistent sodium and slow potassium currents, diagrams have been drawn in parameter space g_{NaP}-g_{KS} (White et al. 1995; Hutcheon and Yarom 2000). In Figure 2, α is proportional to minus g_{NaP}, while β is proportional to g_{KS}. The triangular region (of the above mentioned diagram) where subthreshold oscillations occur corresponds to the area bounded by the line where spontaneous oscillations arise and the continuation of the straight line indicating a zero total conductance in Figure 2. Likewise, the diagram of Manor et al. (1997), showing how the cellular behavior changes when the leak conductance and the conductance of a low-threshold calcium current are changed, is related to Figure 2, by an appropriate change of variables. The conductance of the low threshold calcium channels enters both on the α variable (through its instantaneous activation dynamics) and on the β variable.

Firing-rate dynamics

Resonance properties have traditionally been studied at the single neuron level, or in neurons coupled by gap junctions (Manor et al. 1997). On the other hand, firing properties of resonant neurons have been less systematically studied. Such studies are important to assess the role of resonance in networks in which the main coupling is chemical and not electrical. Indeed, for subthreshold resonant properties to affect network dynamics, as reported by Tiesinga et al. (2001) and Wang (2002), the firing properties of single neurons themselves should be sensitive to the resonance. In the present paper, this question has been investigated, using both reduced models and conductance-based models. It has been shown how noise plays a crucial role in the appearance of resonance at subthreshold frequencies of the firing rate modulated by a sinusoidal input. When noise is weak, and firing is regular, the firing rate response is dominated by resonances at the background firing frequency, and the subthreshold resonance is masked. When noise is strong, and firing is approximately Poisson, the resonance at the background firing rate disappears, and the subthreshold resonance is revealed. The phenomenon is most clearly seen with the GIF model that has a subthreshold response independent of membrane potential and is submitted to white-noise current inputs. This produces a single voltage-independent resonant frequency which can be directly compared with the frequency amplified in the firing rate. Given the simplicity of the model, the shift of the firing rate resonance with noise and its relation to the subthreshold can also be demonstrated mathematically. However, neurons are more realistically modeled using a conductance-based description. In addition, synaptic "noise" is better modeled by conductance fluctuations that both modify the conductance of the neuron and give rise to correlated noise. This complicates the phenomenon as compared to the GIF model. The neuronal conductance and the preferred subthreshold frequency vary with the membrane potential and with the input strengths. The effect of increasing synaptic conductance is to increase the subthreshold resonance frequency, and this effect leads, for noisy inputs, to a corresponding increase in firing rate resonance frequency. The noise correlations also modify the neuronal response at high frequency as previously described (Brunel et al. 2001) but this happens at higher frequencies than those of interest here. So, the phenomenon observed with the GIF model is found to remain true for the conductance-based models. At a general level of explanation, it can be attributed to the band pass filter properties of the membrane subthreshold dynamics, that amplify the response at the subthreshold preferred frequency.

Our study suggests a functional role for noise in making known to the network the frequency preferences of single neurons. In a sense, noise allows the neurons to communicate to each other information about the particular subthreshold ion-channel dynamics they exhibit, a message that otherwise would be lost in regular spiking dynamics. These results on the firing rate dynamics of resonant neurons could be tested in any slice preparation in which resonant neurons are observed. Between $1,000$ to $50,000$ seconds of simulation time were needed to produce accurate numerical data for this paper. However, simulations also suggest that collecting spikes for about 5 to 10 minutes per frequency should be sufficient to see the effects of subthreshold resonance in the signal gain at a reasonable

significance level.

It should perhaps be emphasized that the unmasking of subthreshold resonance properties by noise is quite distinct from the usual "stochastic resonance" effect (Wiesenfeld and Moss 1995) that quantifies the output at a given frequency as the strength of noise is varied. In this case, resonance generally arises as some stochastic rate coincides with the given oscillating frequency. A simple integrate-and-fire model, with passive membrane properties, displays stochastic resonance (Bulsara et al. 1994) but not the subthreshold and firing-rate resonance studied here.

Firing rate resonance and the associated phase advance of the firing rate at low frequencies can also be due to other mechanisms, such as spike frequency adaptation (Fuhrmann et al. 2002). One difference between the two mechanisms is that with spike frequency adaptation the negative feedback comes through action potential-dependent currents, whereas in the case of subthreshold resonance negative feedback comes from the interspike subthreshold dynamics. Another difference is that for the case of subthreshold resonance, the peak response in the signal gain and corresponding zero phase lag near the resonant frequency do not appear under noiseless conditions.

Implications for network synchronization

The firing rate signal gain examined in this paper is one of the crucial quantities that determines the synchronization properties of large networks, together with the temporal characteristics of synaptic transmission. In particular, the existence of phase advance of the firing rate at low frequency can generate an oscillation in networks of excitatory neurons, as was shown for the case of adapting neurons (Fuhrmann et al. 2002). Therefore, we expect that in noisy *in vivo*-like conditions, networks of excitatory neurons with subthreshold resonance could generate oscillations.

From the theoretical point of view, we have introduced a simplified neuronal model for a resonant neuron, the generalized integrate-and-fire neuron, that can be engineered to capture the subthreshold dynamics of any conductance-based model neuron, but with a fixed threshold for firing. Simple one-variable integrate-and-fire neurons have proven very useful for understanding the dynamics of large networks, since analytical tools can be applied to study and understand in great detail the collective dynamics of such networks (see e.g. Amit and Tsodyks 1991; Treves 1993; Abbott and van Vreeswijk 1993; Amit and Brunel 1997; Brunel and Hakim 1999; Gerstner 2000; Brunel 2000). However, integrate-and-fire neurons are clearly not suited to describe neurons with subthreshold resonance. The generalized integrate-and-fire neuron that was introduced here provides an appropriate tool for the investigation of the collective properties of networks of resonant neurons. Such theoretical studies will help to obtain a deeper understanding of the functional role of subthreshold resonance in the nervous system.

Acknowledgments

We would like to thank Ole Paulsen for useful discussions, as well as Claude Meunier and Arnaud Tonnelier for their detailed comments on a previous version of the manuscript. M.J.E.R acknowledges support from a European Community Marie Curie Fellowship. Laboratoire de Physique Statistique is CNRS UMR8550, associé aux Universités Paris VI et VII.

Appendix

Model I: Spiking neuron with an I_H current

The model is defined as follows

$$C_M \frac{dV}{dt} = -I_L - I_H - I_{Na} - I_K - I_{syn} + I_{app}$$

where the membrane capacitance $C_M = 0.37$nF and the leak current I_L is defined by $I_L = \overline{g}_L(V - E_L)$ with $\overline{g}_L = 0.037\mu$S and $E_L = -68$mV. The other currents take the form

$$\begin{aligned} I_{Na} &= \overline{g}_{Na} m_\infty^3 h\,(V - E_{Na}) \\ I_K &= \overline{g}_K n^4 (V - E_K) \\ I_H &= \overline{g}_H (0.8f + 0.2s)(V - E_H) \end{aligned}$$

where the conductances $\overline{g}$ and reversal potentials E are given in table (1) and it should be noted that $f_\infty = s_\infty$. The time-varying activation and inactivation variables h, n, f and s all follow equations of the form

$$\tau_x(V) \frac{dx}{dt} = x_\infty(V) - x. \tag{15}$$

The voltage dependence of the corresponding $\tau_x(V)$ and $x_\infty(V)$ parameters are also given in table (1). All currents are taken to be at physiological temperatures, and hence the timescale of the Hodgkin-Huxley spike-generating currents have been shortened by the temperature factor $\phi = 3^{(36-6.3)/10} = 26.12$. The resting voltage of this model neuron is $V_{rest} = -65.2$mV and the firing threshold is close to -56.4mV.

Linearization. Following the procedure outlined in Methods, the conductance-based model outlined above can be linearized around a holding voltage V^* (which can be varied by changing I_{app}). This model yields the following set of linear equations

$$\begin{aligned} C_M \dot{v} &= -g_M v - g_h w_h - g_n w_n - g_f w_f - g_s w_s, \\ \tau_h \dot{w}_h &= v - w_h \qquad \tau_n \dot{w}_n = v - w_n \\ \tau_f \dot{w}_f &= v - w_f \qquad \tau_s \dot{w}_s = v - w_s \end{aligned}$$

The conductance $g_M = \partial I_{mem}/\partial V$ is the slope of the instantaneous $I - V$ curve at V^*

$$\begin{aligned} g_M &= \overline{g}_L + \overline{g}_{Na} m_\infty^3 h_\infty + \overline{g}_K n_\infty^4 + \overline{g}_H (0.8 f_\infty + 0.2 s_\infty) \\ &\quad + 3\overline{g}_{Na} m_\infty^2 h_\infty (V^* - E_{Na}) \left(\frac{\partial m_\infty}{\partial v}\right)^* \end{aligned}$$

where the convention that X^* is the quantity X evaluated at the holding voltage V^* is used. The other conductances introduced are

$$g_h = \overline{g}_{Na}(V^* - E_{Na}) m_\infty^3 \left(\frac{\partial h_\infty}{\partial v}\right)^* \qquad g_n = 4\overline{g}_K (V^* - E_K) n_\infty^3 \left(\frac{\partial n_\infty}{\partial v}\right)^*$$

current	$\overline{g}$ (μS)	E (mV)	gating variables $\{x_\infty\}$	τ_x (ms)
I_{Na}	19.24	+55	$m_\infty = \alpha_m/(\alpha_m + \beta_m)$	$\tau_m = 0$
			$h_\infty = \alpha_h/(\alpha_h + \beta_h)$	$\tau_h = 1/(\phi(\alpha_h + \beta_h))$
I_K	7.4	−90	$n_\infty = \alpha_n/(\alpha_n + \beta_n)$	$\tau_n = 1/(\phi(\alpha_n + \beta_n))$
I_H	0.03	−41	$f_\infty = 1/(1 + e^{(V+78)/7})$	$\tau_f = 38$
			$s_\infty = 1/(1 + e^{(V+78)/7})$	$\tau_s = 319$
I_{NaP}	0.037	+55	$p_\infty = 1/(1 + e^{-(V+51)/5})$	$\tau_p = 0$
I_{Ks}	2.59	−90	$q_\infty = 1/(1 + e^{-(V+34)/6.5})$	$\tau_q = 6$
$I_{Ks}^{(2)}$	5.18	−90	$q_\infty = 1/(1 + e^{-(V+34)/6.5})$	$\tau_q = 6$
			$k_\infty = 1/(1 + e^{(V+65)/6.6})$	$\tau_k = 200\ + 220/\left(1 + e^{-(V+71.6)/6.85}\right)$

Table 1: The definitions and parameters of the currents used for the conductance-based models.

$$g_f = \overline{g}_H 0.8(V^* - E_H)\left(\frac{\partial f_\infty}{\partial v}\right)^* \qquad g_s = \overline{g}_H 0.2(V^* - E_H)\left(\frac{\partial s_\infty}{\partial v}\right)^*.$$

Reduction to two variables. The variables w_h and w_n are much faster than other timescales in the system. Thus the substitution $w_h = v$ and $w_n = v$ in the voltage equation represents a good approximation. The slow variable of the H current w_s has a relatively long timescale and hence follows the time-average of v (obtained from a solution of equation (15)). For voltage changes that average to zero around the rest, the replacement $w_s \to 0$ is a valid approximation. These approximations taken together yield the two-variable system of equations:

$$\begin{aligned} C\frac{dv}{dt} &= -gv - g_f w_f \\ \tau_f \frac{dw_f}{dt} &= v - w_f \end{aligned}$$

where $C = C_M$ and $g = g_M + g_h + g_n$.

Model II

The model is defined as follows

$$C_M \frac{dV}{dt} = -I_L - I_{NaP} - I_{Ks} - I_{Na} - I_K - I_{syn} + I_{app}$$

where $C_M = 0.37$nF and the leak current is given by $I_L = \overline{g}_L(V - E_L)$ with $\overline{g}_L = 0.037\mu$S and $E_L = -60$mV. The spike generating currents are identical to those of Model I. The I_{NaP} and non-inactivating I_{Ks} currents are defined by

$$\begin{aligned} I_{NaP} &= \overline{g}_{NaP} p_\infty (V - E_{NaP}) \\ I_{Ks} &= \overline{g}_{Ks} q (V - E_{Ks}). \end{aligned}$$

	α	β
m	$\alpha_m = \frac{-0.1(V+32)}{\exp(-0.1(V+32))-1}$	$\beta_m = 4\exp(-(V+57)/18)$
h	$\alpha_h = 0.07\exp(-(V+46)/20)$	$\beta_h = \frac{1}{\exp(-0.1(V+16))+1}$
n	$\alpha_n = \frac{-0.01(V+36)}{\exp(-0.1(V+36))-1}$	$\beta_n = 0.125\exp(-(V+46)/80)$

Table 2: The values for α and β used in the definition of the spike-generating currents I_{Na} and I_K.

The resting voltage of the neuron is $V_{rest} = -66.2\text{mV}$ and the onset of spontaneous oscillations occurs near -57.2mV.

Linearization. Linearizing this model at a fixed voltage V^* yields the following set of linear differential equations

$$\begin{aligned} C\dot{v} &= -g_M v - g_h w_h - g_n w_n - g_q w_q \\ \tau_h \dot{w_h} &= v - w_h \qquad \tau_n \dot{w_n} = v - w_n \\ \tau_q \dot{w_q} &= v - w_q \end{aligned}$$

where again the conductance $g_M = \partial I_{mem}/dV$ is the slope of the instantaneous $I-V$ curve at V^*

$$\begin{aligned} g_M &= \overline{g}_L + \overline{g}_{Na} m_\infty^3 h_\infty + \overline{g}_K n_\infty^4 + \overline{g}_{NaP} p_\infty + \overline{g}_{Ks} q_\infty \\ &\quad + 3\overline{g}_{Na} m_\infty^2 h_\infty (V^* - E_{Na}) \left(\frac{\partial m_\infty}{\partial v}\right)^* + \overline{g}_{NaP}(V - E_{Na}) \left(\frac{\partial p_\infty}{\partial v}\right)^* \end{aligned}$$

and the other conductance not common to model I is

$$g_q = \overline{g}_{Ks}(V - E_K) \left(\frac{\partial q_\infty}{\partial v}\right)^*$$

where all voltage-dependent quantities are evaluated at V^*.

Reduction to two variables. Again the model can be reduced to the two-variable form by noting that the timescales of the spike-generating currents are much faster than other timescales in the voltage equation. However, in this case the replacements $w_h = v - g_h \tau_h \dot{v}$ and $w_n = v - g_n \tau_n \dot{v}$ are used, giving a better agreement near the line where spontaneous oscillations appear. Thus the two-variable reduction of this model is

$$\begin{aligned} C\frac{dv}{dt} &= -vg - g_q w_q \\ \tau_q \frac{dw_q}{dt} &= v - w_q \end{aligned} \tag{16}$$

where $C = C_M - g_h\tau_h - g_n\tau_n$ and $g = g_M + g_h + g_n$.

Model with a trough in the impedance

This model is similar to Model II defined above, except that in this case an inactivation term is included in the definition of the slow potassium current

$$I_{Ks}^{(2)} = \overline{g}_{Ks} q k (V - E_K)$$

see table (1) for the values of the various parameters. This model is linearized around -65mV to give the following set of equations

$$\begin{aligned} C\dot{v} &= -g_M v - g_h w_h - g_n w_n - g_q w_q - g_k w_k \\ \tau_h \dot{w_h} &= v - w_h \qquad \tau_n \dot{w_n} = v - w_n \\ \tau_q \dot{w_q} &= v - w_q \qquad \tau_k \dot{w_k} = v - w_k \end{aligned}$$

where in this case

$$\begin{aligned} g_M &= \overline{g}_{Na} m_\infty^3 h_\infty + \overline{g}_K n_\infty^4 + \overline{g}_{NaP} p_\infty + \overline{g}_{Ks} q_\infty k_\infty \\ &\quad + \overline{g}_{NaP} (V - E_{Na}) \left(\frac{\partial p_\infty}{\partial v} \right)^* + 3 \overline{g}_{Na} m_\infty^2 h_\infty (V^* - E_{Na}) \left(\frac{\partial m_\infty}{\partial v} \right)^* \end{aligned}$$

and

$$g_k = \overline{g}_{Ks} (V - E_K) q_\infty \left(\frac{\partial k_\infty}{\partial v} \right)^* \qquad g_q = \overline{g}_{Ks} (V - E_K) k_\infty \left(\frac{\partial q_\infty}{\partial v} \right)^* .$$

The corresponding three-variable model is found by assuming the h and n variables are fast, leaving the set

$$\begin{aligned} C\dot{v} &= -gv - g_q w_q - g_k w_k \\ \tau_q \dot{w_q} &= v - w_q \qquad \tau_k \dot{w_k} = v - w_k, \end{aligned}$$

where $C = C_M - g_h \tau_h - h_n \tau_n$ and $g_M = g + g_n + g_h$.

The two-variable approximation of this model is obtained by the further assumption that the k variable is slow, and hence w_k is set to zero. At $V^* = -65$mV this two-variable model is identical to that of Model II given above. The impedance curves of the full, three and two-variables models are given in Figure 3B.

Impedance and eigenvalues of the two-variable model

The eigenvalues of the two-variable model are

$$\begin{aligned} \lambda_1 &= \frac{1}{2\tau_1} \left(-(\alpha + 1) + \sqrt{(\alpha - 1)^2 - 4\beta} \right) \\ \lambda_2 &= \frac{1}{2\tau_1} \left(-(\alpha + 1) - \sqrt{(\alpha - 1)^2 - 4\beta} \right) \end{aligned} \tag{17}$$

Stability of the membrane potential. For the membrane potential to be stable, the real part of both eigenvalues must be negative. This gives the following bounds on the parameters α and β:

$$\alpha > -1 \quad \text{and} \quad \alpha + \beta > 0. \tag{18}$$

Amplitude of the impedance. For an oscillating current of frequency $f = \omega/(2\pi)$ the amplitude of the complex impedance $|Z|$ is given as

$$|Z| = \left(\frac{\tau_1}{C}\right)\sqrt{\frac{(1+\tau_1^2\omega^2)}{(\alpha+\beta-\tau_1^2\omega^2)^2+\tau_1^2\omega^2(1+\alpha)^2}}. \tag{19}$$

A subthreshold resonance, signaled by the existence of peak in $|Z(f)|$ at some non-zero frequency, occurs if (Hutcheon et al. 1996a)

$$\beta > \sqrt{(\alpha+1)^2+1} - (1+\alpha)$$

and at a frequency

$$f_R = \frac{1}{2\pi\tau_1}\left(\left((\alpha+\beta+1)^2-(\alpha+1)^2\right)^{1/2}-1\right)^{1/2}. \tag{20}$$

The phase of the impedance. The phase θ, defined in equation (11), is

$$\tan(\theta) = \tau_1\omega\frac{\beta-(1+\tau_1^2\omega^2)}{\beta+\alpha(1+\tau_1^2\omega^2)} \tag{21}$$

A zero phase-lag exists for $\beta > 1$, while a phase lag greater than 90 degrees is present for $\alpha < 0$.

Response to a square-pulse current. The response of the neuron to the onset of a square-pulse current $I_{app} = I\Theta(t)$ can be found in terms of the eigenvalues as

$$v = v_\infty + v_\infty\left(e^{\lambda_1 t}\left(\frac{\tau_1\lambda_1\lambda_2+\lambda_2}{\lambda_1-\lambda_2}\right)+e^{\lambda_2 t}\left(\frac{\tau_1\lambda_1\lambda_2+\lambda_1}{\lambda_2-\lambda_1}\right)\right)$$

where $v_\infty = I/(g+g_1)$ is the holding voltage corresponding to an applied current of $I_{app} = I$ in the linear approximation. When the roots are complex, and written as $\lambda = -\mu \pm \omega_0$ the form above can be written more conveniently as

$$v = v_\infty - v_\infty e^{-\mu t}\left(\cos(\omega_0 t)+\left(\frac{\mu-\tau_1(\mu^2+\omega_0^2)}{\omega_0}\right)\sin(\omega_0 t)\right).$$

The existence of complex eigenvalues indicates that the neuron has damped oscillations at a frequency f_0. This occurs when $4\beta > (\alpha-1)^2$ (Puil et al. 1986) giving

$$\omega_0 = \frac{1}{2\tau_1}\sqrt{4\beta-(\alpha+1)^2}. \tag{22}$$

The qualitatively different types of behavior that can occur are the following: When $\beta > (\alpha-1)^2/4$ the membrane response with damped oscillations; When $\alpha > 1$ and $0 < \beta < (\alpha-1)^2/4$ the membrane has a single overshoot (or sag if the current pulse is hyperpolarizing); For all other cases $\alpha < 1$, $\beta < (\alpha-1)^2/4$ and $\alpha > 1$, $\beta < 0$ the voltage changes monotonically from its initial to final value.

Impedance and eigenvalues of the three-variable model

The complex impedance of the three-variable model model defined by equations 7 is

$$Z = \frac{1}{g}\left(\frac{(1+i\omega\tau_1)(1+i\omega\tau_2)}{(1+i\omega\tau_m)(1+i\omega\tau_1)(1+i\omega\tau_2)+\gamma_1(1+i\omega\tau_2)+\gamma_2(1+i\omega\tau_1)}\right) \quad (23)$$

where $\omega = 2\pi f$, $\tau_m = C/g$, $\gamma_1 = g_1/g$, and $\gamma_2 = g_2/g$.

To classify the behavior of the amplitude of the impedance vs frequency curve in terms of the number of local minima and/or maxima, the derivative of $|Z|$ with respect to ω is computed. Its sign is determined by a fourth order polynomial in ω^2. The number of real positive roots of this polynomial tell us how many local extrema there are in the amplitude vs frequency curve. The roots of the polynomial are found numerically. From these roots, the boundaries of the regions with 0, 1 or 2 local minima, corresponding respectively to no resonance, simple resonance, and resonance preceded by a trough, are found numerically.

The eigenvalues of the stability matrix of equations (7) are given by the following cubic polynomial

$$\lambda^3 + \left(\frac{1}{\tau_m}+\frac{1}{\tau_1}+\frac{1}{\tau_2}\right)\lambda^2 + \left(\frac{1}{\tau_1\tau_2}+\frac{1+\gamma_1}{\tau_1\tau_m}+\frac{1+\gamma_2}{\tau_2\tau_m}\right)\lambda + \frac{1+\gamma_1+\gamma_2}{\tau_1\tau_2\tau_m} = 0 \quad (24)$$

Insertion of $\lambda = 0$ in equation (24) yields the line $1+\gamma_1+\gamma_2 = 0$. To find the line where spontaneous oscillations appear, we set $\lambda = i\omega$, and obtain a half straight line in a parametric way

$$\begin{aligned}\gamma_1 &= \frac{\tau_m+\tau_2}{\tau_1-\tau_2}(1+\omega^2\tau_1^2)\\ \gamma_2 &= -\frac{\tau_m+\tau_1}{\tau_1-\tau_2}(1+\omega^2\tau_2^2)\end{aligned}$$

Finally, to obtain the regions where damped oscillatory behavior arise in response to a step current, the roots of the cubic polynomial are computed numerically. The boundaries of the area in which a pair of complex conjugate roots appear are then found.

Calculation of the firing-rate resonance

The modulation in the instantaneous firing rate due to a sinusoidal input in the limit $\tau_1 \gg \tau$ can be calculated analytically. Details will be published elsewhere (Brunel, Hakim

and Richardson, in preparation). The modulation in the firing rate can be written

$$\begin{aligned} A(\omega) &= \left(1 - \frac{\gamma Y(\omega)}{1 + \gamma Y(\omega) + i\omega\tau_1}\right) A_{LIF}(\omega) \\ Y(\omega) &= \frac{1 - g\tau_m(v_\theta - v_r)A_{LIF}(\omega)}{1 + i\omega\tau_m} \end{aligned}$$

where $\gamma = g_1/g$, $\tau_m = C/g$ and $A_{LIF}(\omega)$ is the firing-rate linear response (signal gain) of the integrate-and-fire neuron (Brunel and Hakim 1999; Brunel et al. 2001),

$$A_{LIF}(\omega) = \frac{r_0}{g\sigma(1 + i\omega\tau_m)} \left(\frac{\frac{\partial U}{\partial y}(y_t, \omega\tau_m) - \frac{\partial U}{\partial y}(y_r, \omega\tau_m)}{U(y_t, \omega\tau_m) - U(y_r, \omega\tau_m)} \right), \tag{25}$$

the noise strength here is given by $\sigma = (I_N/g)\sqrt{\tau_N/\tau_m}$. The parameters y_t, y_r and the background firing rate r_0 are given by the set of equations

$$\begin{aligned} y_t &= \frac{v_\theta + \gamma\langle v\rangle - I_0/g}{\sigma} \\ y_r &= \frac{v_r + \gamma\langle v\rangle - I_0/g}{\sigma}, \\ \langle v\rangle &= \frac{I_0/g - (v_\theta - v_r)r_0\tau_m}{1 + \gamma}, \\ r_0 &= \left(\tau_m\sqrt{\pi}\int_{y_r}^{y_t} e^{u^2}\left[1 + \mathrm{erf}(u)\right]\right)^{-1} \end{aligned} \tag{26}$$

where $\mathrm{erf}(u)$ is the standard error function, and U is given in terms of combinations of hypergeometric functions (Abramowitz and Stegun 1970)

$$U(y, w) = \frac{e^{y^2}}{\Gamma\left((1 + iw)/2\right)} M\left(\frac{1 - iw}{2}, \frac{1}{2}, -y^2\right) + \frac{2ye^{y^2}}{\Gamma\left(iw/2\right)} M\left(1 - \frac{iw}{2}, \frac{3}{2}, -y^2\right). \tag{27}$$

The amplitudes of the signal-gain profiles $|A(f)|$ in Figures (6) and (7) have been normalized to 1 at zero frequency for both the analytical results (bold lines) and data from numerical simulation (symbols). A systematic and frequency-independent shift of about 10% between theory and numerics was visible in the unnormalized curves due to the finite value of τ_1. Such a shift can be captured analytically by examining higher orders of the approximation that take the finite value of τ_1 into account.

References

Abbott, L. F. and C. van Vreeswijk (1993). Asynchronous states in a network of pulse-coupled oscillators. *Phys. Rev. E 48*, 1483–1490.

Abramowitz, M. and I. A. Stegun (1970). *Tables of mathematical functions*. Dover Publications, NY.

Adrian, E. D. and B. H. C. Matthews (1934). The Berger rhythm: potential changes from the occipital lobes in man. *Brain 57*, 355–385.

Amit, D. J. and N. Brunel (1997). Model of global spontaneous activity and local structured activity during delay periods in the cerebral cortex. *Cerebral Cortex 7*, 237–252.

Amit, D. J. and M. V. Tsodyks (1991). Quantitative study of attractor neural network retrieving at low spike rates I: Substrate – spikes, rates and neuronal gain. *Network 2*, 259–274.

Anderson, J. S., I. Lampl, D. C. Gillespie, and D. Ferster (2000). The contribution of noise to contrast invariance of orientation tuning in cat visual cortex. *Science 290*, 1968–1972.

Brunel, N. (2000). Dynamics of sparsely connected networks of excitatory and inhibitory spiking neurons. *J. Comput. Neurosci. 8*, 183–208.

Brunel, N., F. Chance, N. Fourcaud, and L. Abbott (2001). Effects of synaptic noise and filtering on the frequency response of spiking neurons. *Phys. Rev. Lett. 86*, 2186–2189.

Brunel, N. and V. Hakim (1999). Fast global oscillations in networks of integrate-and-fire neurons with low firing rates. *Neural Computation 11*, 1621–1671.

Bulsara, A. R., S. B. Lowen, and C. D. Rees (1994). Cooperative behavior in the periodically modulated wiener process: Noise-induced complexity in a model neuron. *Phys. Rev. E 49*, 4989–5000.

De Zeeuw, C. I., J. I. Simpson, C. C. Hoogenraad, N. Galjart, S. K. Koekkoek, and T. J. Ruigrok (1998). Microcircuitry and function of the inferior olive. *TINS 21*, 391–400.

Destexhe, A. and D. Paré (1999). Impact of network activity on the integrative properties of neocortical pyramidal neurons in vivo. *J. Neurophysiol. 81*, 1531–1547.

Destexhe, A., M. Rudolph, J.-M. Fellous, and T. J. Sejnowski (2001). Fluctuating synaptic conductances recreate *in vivo*-like activity in neocortical neurons. *Neuroscience 107*, 13–24.

Dickson, C. T., J. Magistretti, M. H. Shalinsky, E. Fransen, M. E. Hasselmo, and A. Alonso (2000). Properties and role of I(h) in the pacing of subthreshold oscillations in entorhinal cortex layer II neurons. *J. Neurophysiol. 83*, 2562–2579.

Fuhrmann, G., H. Markram, and M. Tsodyks (2002). Spike frequency adaptation and neocortical rhythms. *J. Neurophysiol. 88*, 761-770.

Gerstner, W. (2000). Population dynamics of spiking neurons: fast transients, asynchronous states, and locking. *Neural Computation 12*, 43–89.

Gutfreund, Y., Y. Yarom, and I. Segev (1995). Subthreshold oscillations and resonant frequency in guinea-pig cortical neurons: physiology and modelling. *J. Physiol. 483*, 621–640.

Hodgkin, A. L. and A. F. Huxley (1952). A quantitative description of membrane current and its application to conductance and excitation in nerve. *J. Physiol. 117*, 500–544.

Honeycutt, R. L. (1992). Stochastic Runge-Kutta algorithms. I. White noise. *Phys. Rev. A 45*, 600–603.

Hutcheon, B., R. M. Miura, and E. Puil (1996a). Models of subthreshold membrane resonance in neocortical neurons. *J. Neurophysiol. 76*, 698–714.

Hutcheon, B., R. M. Miura, and E. Puil (1996b). Subthreshold membrane resonance in neocortical neurons. *J. Neurophysiol. 76*, 683–697.

Hutcheon, B., R. M. Miura, Y. Yarom, and E. Puil (1994). Low-threshold calcium current and resonance in thalamic neurons: a model of frequency preference. *J. Neurophysiol. 76*, 683–697.

Hutcheon, B. and Y. Yarom (2000). Resonance, oscillation and the intrinsic frequency preferences of neurons. *TINS 23*, 216–222.

Izhikevich, E. M. (2001). Resonate-and-fire neurons. *Neural Networks 14*, 883–894.

Jahnsen, H. and S. Karnup (1994). A spectral analysis of the integration of artificial synaptic potentials in mammalian central neurons. *Brain Research 666*, 9–20.

Knight, B. W. (1972). The relationship between the firing rate of a single neuron and the level of activity in a population of neurons. *J. Gen. Physiol. 59*, 767–778.

Koch, C. (1984). Cable theory in neurons with active linearized membrane. *Biol. Cybern. 50*, 15–33.

Koch, C. (1999). *Biophysics of computation: information processing in single neurons.* Oxford University Press.

Lampl, I. and Y. Yarom (1993). Subthreshold oscillations of the membrane potential: a functional synchronizing and timing device. *J. Neurophysiol. 70*, 2181–2186.

Lampl, I. and Y. Yarom (1997). Subthreshold oscillations and resonant behavior: two manifestations of the same mechanism. *Neuroscience 78*, 325–341.

Leung, L. S. and H. W. Yu (1998). Theta-frequency resonance in hippocampal CA1 neurons *in vitro* demonstrated by sinusoidal current injection. *J. Neurophysiol. 79*, 1592–1596.

Llinás, R., A. A. Grace, and Y. Yarom (1991). *In vitro* neurons in mammalian cortical layer 4 exhibit intrinsic oscillatory activity in he 10- to 50-hz frequency range. *Proc. Natl. Acad. Sci. U.S.A. 88*, 897–901.

Llinás, R. and Y. Yarom (1986). Oscillatory properties of guinea pig olivary neurons and their pharmacological modulation: an *in vitro* study. *J. Physiol. 376*, 163–182.

Manor, Y., J. Rinzel, I. Segev, and Y. Yarom (1997). Low-amplitude oscillations in the inferior olive: A model based on electrical coupling of neurons with heterogeneuos channel densitites. *J. Neurophysiol. 77*, 2736–2752.

Mauro, A., F. Conti, F. Dodge, and R. Schor (1970). Subthreshold behavior and phenomenological impedance of the squid giant axon. *J. Gen. Physiol. 55*, 497–523.

Pike, F. G., R. S. Goddard, J. M. Suckling, P. Ganter, N. Kasthuri, and O. Paulsen (2000). Distinct frequency preferences of different types of rat hippocampal neurones in response to oscillatory input currents. *J. Physiol. 529*, 205–213.

Puil, E., B. Gimbarzevsky, and R. M. Miura (1986). Quantification of membrane properties of trigeminal root ganglions in guinea pigs. *J. Neurophysiol. 55*, 995–1016.

Puil, E., H. Meiri, and Y. Yarom (1994). Resonant behavior and frequency preferences of thalamic neurons. *J. Neurophysiol. 71*, 575–582.

Rinzel, J. and G. B. Ermentrout (1989). Analysis of neural excitability and oscillations. In *Methods in Neuronal Modeling*, pp. 135–169. MIT press, Cambridge, MA.

Spain, W. J., P. C. Schwindt, and W. E. Crill (1987). Anomalous rectification in neurons from cat sensorimotor cortex in vitro. *J. Neurophysiol. 57*, 1555–1576.

Tiesinga, P. H., J. M. Fellous, J. V. Jose, and T. J. Sejnowski (2001). Computational model of carbachol-induced delta, theta, and gamma oscillations in the hippocampus. *Hippocampus 11*, 251–274.

Treves, A. (1993). Mean-field analysis of neuronal spike dynamics. *Network 4*, 259–284.

Wang, X. J. (1993). Ionic basis for intrinsic oscillations. *NeuroReport 5*, 221–224.

Wang, X.-J. (2002). Pacemaker neurons for the theta rhythm and their synchronization in the septohippocampal reciprocal loop. *J. Neurophysiol. 87*, 889–900.

White, J. A., T. Budde, and A. R. Kay (1995). A bifurcation analysis of neuronal subthreshold oscillations. *Biophys. J. 69*, 1203–1217.

Wiesenfeld, K. and F. Moss (1995). Stochastic resonance and the benefits of noise: from ice ages to crayfish and squids. *Nature 373*, 33–36.